Fe0/FeO/ultra-stable Y zeolite for energy-efficient solar photo-Fenton degradation and mineralization of chloramphenicol in aqueous matrices

Original
Fe0/FeO/ultra-stable Y zeolite for energy-efficient solar photo-Fenton degradation and mineralization of chloramphenicol in aqueous matrices / Morante, Nicola; Marocco, Antonello; Monfreda, Viviana; Padua, Alessandro; Sisti, Mattia; Arletti, Rossella; Sannino, Diana; Pansini, Michele; Esposito, Serena; Vaiano, Vincenzo. - In: JOURNAL OF WATER PROCESS ENGINEERING. - ISSN 2214-7144. - 79:(2025). [10.1016/j.jwpe.2025.108938]

Publisher:
ELSEVIER

Published
DOI:10.1016/j.jwpe.2025.108938

Journal of Water Process Engineering 79 (2025) 108938

Contents lists available at ScienceDirect

Journal of Water Process Engineering

journal homepage: www.elsevier.com/locate/jwpe

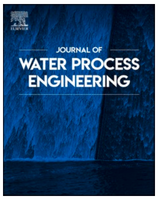

Fe^0/Fe$_3$O$_4$/ultra-stable Y zeolite for energy-efficient solar photo-Fenton degradation and mineralization of chloramphenicol in aqueous matrices

Nicola Morante [a,1], Antonello Marocco [b,1], Viviana Monfreda [b], Alessandro Padua [c], Mattia Sisti [d], Rossella Arletti [d], Diana Sannino [a], Michele Pansini [b], Serena Esposito [c,*], Vincenzo Vaiano [a,*]

[a] *Department of Industrial Engineering, University of Salerno, Via Giovanni Paolo II 132, 84084 Fisciano, (SA), Italy*
[b] *Department of Civil and Mechanical Engineering and INSTM Research Unit, Università degli Studi di Cassino e del Lazio Meridionale, Via G. Di Biasio 43, Cassino, FR, 03043, Italy*
[c] *Department of Applied Science and Technology and INSTM Unit of Torino – Politecnico, Politecnico di Torino, Corso Duca degli Abruzzi 24, 10129, Torino, Italy*
[d] *Università degli Studi di Modena e Reggio Emilia, Chemical and Geological Sciences, Via Campi 103, Modena, 41125, Italy*

ARTICLE INFO

Editor: Ludovic F. Dumée

Keywords:
Fe^0/Fe$_3$O$_4$/USY
Ultrastable Y zeolites
Chloramphenicol
Photo-Fenton
Solar light

ABSTRACT

Ultrastable Y (USY) zeolites with different Si/Al ratios were used as a support for Fe^0 and Fe$_3$O$_4$, loaded via vacuum impregnation of ferrous solutions followed by thermal treatment in a reducing atmosphere. The influence of Fe^0/Fe$_3$O$_4$ ratios in the magnetically recoverable Fe^0/Fe$_3$O$_4$/USY composite catalysts was explored in the solar-assisted photo-Fenton degradation of chloramphenicol (CAP), a recalcitrant antibiotic frequently detected in pharmaceutical wastewater.

Under optimized conditions (pH = 4, H_2O_2 dosage = 0.12 g L^{-1}, catalyst loading = 1.5 g L^{-1}), the Fe^0(3.3 %)/Fe$_3$O$_4$(1.6 %)/USY catalyst achieved 98 % CAP degradation within 30 min in the dark and 52 % TOC removal after 120 min under simulated solar irradiation. Scavenger and band structure analyses revealed that hydroxyl radicals were the primary oxidative species responsible for CAP degradation. The catalyst exhibited excellent reusability and maintained high activity in the presence of common inorganic ions present in real water matrix, confirming its robustness under realistic water treatment conditions.

A comparative energy consumption analysis demonstrated that the proposed system requires significantly lower energy input compared to similar photocatalytic and photo-Fenton processes reported in the literature. These findings highlight the potential of Fe^0/Fe$_3$O$_4$/USY as a cost-effective and sustainable solution for the removal of emerging pharmaceutical contaminants from aqueous environments.

1. Introduction

The widespread occurrence of pharmaceutical residues in aquatic ecosystems has emerged as a pressing global concern, with antibiotics among the most frequently detected micro-pollutants. Notably, chloramphenicol (CAP), a broad-spectrum antibiotic banned or restricted in many countries due to its potential to cause aplastic anemia and mutagenic effects, continues to be detected in surface water, groundwater, and wastewater treatment effluents, posing ecological and human health risks [1]. Its high chemical stability and low biodegradability make it particularly persistent, challenging the efficiency of conventional treatment methods, such as biological oxidation [2]. On the other hand, alternative processes also present significant drawbacks. For instance, chlorination can lead to the formation of potentially toxic halogenated by-products [3], while adsorption techniques, although effective in removing CAP from water, do not achieve mineralization and necessitate subsequent handling and disposal of the saturated adsorbent material [4]. These limitations have stimulated interest in developing more robust and efficient treatment strategies, particularly advanced oxidation processes (AOPs), which have demonstrated the potential for complete degradation and mineralization of CAP and other recalcitrant pharmaceuticals [5,6]. Among AOPs, heterogeneous photocatalysis and photo-Fenton systems have shown promising capabilities for the degradation of CAP. Recent studies have reported the effective

---

[*] Corresponding authors.
E-mail addresses: serena_esposito@polito.it (S. Esposito), vvaiano@unisa.it (V. Vaiano).

[1] These authors contributed equally.

https://doi.org/10.1016/j.jwpe.2025.108938
Received 18 August 2025; Received in revised form 2 October 2025; Accepted 14 October 2025

degradation of CAP using a variety of visible-light-active photocatalysts, such as $SrFeO_3/g\text{-}C_3N_4$ heterojunctions [7], $Cu_2O/Cu/g\text{-}C_3N_4$ hybrids [8], and doped Bi_5O_7I microspheres [9]. Other systems, such as nanostructured ZnO thin films and $CeMoO_4$/graphene composites, have also demonstrated activity under UV–visible light [10,11].

Despite these advances, many photocatalytic systems suffer from limitations such as low mineralization efficiency. In this context, the photo-Fenton process offers an attractive alternative. By coupling H_2O_2 with Fe^{2+} ions under solar or UV light, this process generates hydroxyl radicals (•OH) capable of oxidizing recalcitrant organic molecules like CAP. Several studies have demonstrated the efficacy of both homogeneous and heterogeneous photo-Fenton systems for CAP degradation [12,13]. Iron-containing ceramics and hybrid supports have also been explored for their visible-light activity and robustness [14].

Nevertheless, the homogeneous photo-Fenton process is restricted by the need for acidic conditions (typically $pH < 4$), the formation of iron sludge, and continuous iron dosing, which limit its practical implementation [15,16]. To overcome these drawbacks, heterogeneous photo-Fenton systems based on solid iron catalysts have been developed. These systems offer multiple advantages, including catalyst reusability and broader pH applicability. In particular, iron oxides such as magnetite (Fe_3O_4), due to their mixed Fe^{2+}/Fe^{3+} valence states and narrow band gap (~2.2 eV), are capable of both Fenton-like and photocatalytic activity under UV–visible light [17,18]. Zero-valent iron (Fe^0), on the other hand, is capable of promoting the reductive dehalogenation of halogenated organic contaminants through electron transfer reactions in the absence of light [19–23]. Therefore, the combined use of Fe^0 and Fe_3O_4 in a hybrid system offers the potential to synergistically harness both reductive and oxidative degradation pathways, enabling enhanced contaminant removal through photo-Fenton-like processes.

Using ultrastable zeolites (USY) as supports for iron (Fe) and magnetite (Fe_3O_4) nanoparticles in pollutant photodegradation offers significant advantages over conventional zeolites, especially when considering the thermal treatments required to obtain reduced iron phases.

The primary benefit lies in their enhanced structural, thermal, and hydrothermal stability. Conventional zeolites, particularly those with lower silicon to aluminum (Si/Al) ratios, often undergo dealumination, a loss of aluminum atoms from their crystalline framework when exposed to heat, steam, or acidic conditions. This is a critical issue because to achieve reduced iron phases (like Fe^0 or Fe_3O_4 species), the zeolite-supported material typically needs to be subjected to thermal treatment, often at temperatures of at least 450 °C. At these elevated temperatures, conventional zeolites can experience a drastic loss of surface area, a partial collapse of their porous structure, a reduction in critical acidic sites (essential for interacting with iron nanoparticles and pollutants), and a significant decrease in pore volume [24,25].

In contrast, ultrastable zeolites are specifically engineered to withstand such harsh conditions. They are manufactured through a controlled dealumination process, often involving high-temperature hydrothermal treatment, which not only makes them inherently more stable but also intentionally modifies their structure, creating additional mesoporosity within their original microporous framework. This enhanced stability and mesoporosity provide several specific benefits when thermal reduction is required.

In this perspective, ultrastable Y zeolites (USY) are chemically stable and possess large pore volumes, making them ideal platforms for developing efficient heterogeneous catalysts [26].

However, few studies have systematically explored the synergy between Fe^0 and Fe_3O_4 supported on USY zeolite structures, particularly under real sunlight and in water matrices that include competitive inorganic ions such as chloride, nitrate, and phosphate, which can scavenge radicals or block active sites.

In this work, we report on Fe^0/Fe_3O_4/USY composite catalysts developed for the solar heterogeneous photo-Fenton degradation of chloramphenicol. The work evaluates the contribution of both iron phases to CAP degradation and mineralization performance, explores the effect of operational parameters such as catalyst dosage, H_2O_2 concentration, and pH, and investigates catalyst stability over multiple reuse cycles. Special emphasis is placed on the impact of real water matrix constituents such as chloride, phosphate, and nitrate on photocatalytic efficiency. Furthermore, the degradation mechanism is elucidated through scavenger tests and band structure calculations, while the specific electrical energy consumption is estimated and benchmarked against literature values to assess the sustainability of the process. This integrated approach aims to advance the practical implementation of solar-driven heterogeneous photo-Fenton technologies for the removal of recalcitrant antibiotics from water.

2. Materials and methods

2.1. Materials

Tosoh Corporation ultrastable Y zeolite HSZ-360HUA (Si/Al molar ratio = 6.9) and HSZ-390HUA (Si/Al molar ratio = 385), hereafter simply labeled USY360 and USY390, respectively, were used as base materials in the preparation of the catalysts. The standard solutions and the solvents used for the analytical determinations were all Carlo Erba HPLC grade. The solution, whereby USY360 and USY390 zeolites were impregnated, was prepared by using $FeSO_4 \cdot 7H_2O$ (Aldrich, 99.5 %) and doubly distilled water (Carlo Erba reagent grade). The H_2/Ar gas mixture (H_2 3 % volume), used to create the reducing atmosphere during the thermal treatments (4MS023BB product code), was supplied by Nippon Gases.

2.2. Preparation of the impregnating solution

An aqueous solution of ferrous sulfate heptahydrate was used to impregnate USY360 and USY390 zeolites. This solution was prepared as follows: 17.65 g of $FeSO_4 \cdot 7H_2O$ were dissolved in 300 ml of doubly distilled water at ≈7 °C, under continuous stirring and argon bubbling. These precautions were taken to prevent Fe^{2+} oxidation to Fe^{3+} during the impregnation procedure [27].

2.3. Preparation of Fe^0/Fe_3O_4/USY composite catalysts

The USY360 and USY390 zeolites (framework type FAU [28]) underwent the same vacuum impregnation process, which is hereafter described. Specifically, 30 g of zeolite were deposited on the bottom of a glass desiccator having an inner diameter of about 18 cm. The desiccator was equipped with a sealed lid with a two-way stopcock. This apparatus allowed to perform easily the following sequence of operations. The air present in the desiccator and in the porous structure of the USY360 and USY390 zeolites, contained therein, was removed by using a Carpanelli electric pump, model MM56P2, 0.15 kW, 3360 rpm. After approximately 2 h of evacuation, the stopcock connected to the pump was closed and the pump was turned off. Subsequently, the desiccator was filled with 300 ml of the freshly prepared ferrous sulfate heptahydrate solution, previously described. This operation was carried out by opening the second stopcock while maintaining the vacuum conditions, which gives rise to a liquid suction owing to the depression. The 300 ml of such solution, which entered the desiccator, were sufficient to create a head of about one centimeter of liquid above the solid on the bottom. After a few minutes, the tap was opened to allow air to enter the desiccator. Accordingly, a good contact between the liquid and the outer surface and the inner porosity of the zeolite grains was obtained. This contact was protracted for 48 h.

Finally, the water was gradually removed by evaporation according to the following procedure. The open desiccator, containing the zeolites and the impregnating solution, was set in a furnace whose temperature was regulated at 30 °C. After about a day at 30 °C, the temperature of the furnace was raised to 40 °C, and another day had elapsed. Subsequently, the temperature of the furnace was raised to 50 °C and another day elapsed in these conditions. Finally, the temperature of the furnace was raised to 60 °C and about another day elapsed in these conditions. This procedure of slow evaporation was adopted to make sure that all the 17.65 g of $FeSO_4{\cdot}7H_2O$ impregnated the zeolites and would not be brought away by too violent and fast evaporation.

The obtained powders were subjected to ball milling (with a single sphere) for 2 h. The materials obtained according to the described impregnation procedure were named Fe-USY360 and Fe-USY390.

Proper amounts of Fe-USY360 and Fe-USY390 iron impregnated zeolites were set in high-density Al_2O_3 vessels to prepare the catalysts. Then, such vessels were placed in a furnace equipped with a closed porosity Al_2O_3 tubular chamber (length = 91 cm, diameter = 6.9 cm), which was heated at 15 °C/min, under a reducing atmosphere created by a flow of a gaseous mixture H_2/Ar (H_2 3 % volume). A sample of Fe-USY360 zeolite was heated at 500 °C and kept at this temperature for 2 h. As far as FeUSY390 zeolite is concerned, two different catalysts were produced. A first one by heating a sample of FeUSY390 zeolite at 450 °C and keeping it at this temperature for 2 h, and a second one by heating a sample of FeUSY390 zeolite at 500 °C and keeping it at this temperature for 2 h. Once the 2 h of thermal treatment had gone by, the heating system of the furnace was switched off, and the prepared catalysts were allowed to freely cool down to room temperature in the closed furnace. These catalysts were labeled with the following acronyms, which remind the zeolite and thermal treatment used: FeUSY360–500C-2 h, FeUSY390–450C-2 h, and FeUSY390–500C-2 h.

2.4. *Characterization of the Fe^0/Fe_3O_4/USY composite catalysts*

The Fe content of the FeUSY impregnated zeolite was determined as follows. A weighed sample of the FeUSY zeolite was dissolved in an aqueous solution of hydrofluoric and perchloric acid, and the Fe concentration of the solution was determined by spectrophotometry of atomic absorption (Perkin-Elmer Analyst 100).

Powder X-ray diffraction (XRD) analysis was performed using a Philips X'Pert diffractometer with copper Kα radiation. Data were collected over a 2θ range of 5° to 90° with a step size of 0.026° and a counting time of 140 s per step, scan speed (°/s) = 0.0477.

To avoid the well-known issue of Fe fluorescence that occurs when analyzing Fe-rich powders using Cu Kα radiation, a more accurate quantitative phase analysis (QPA) was carried out on selected samples using synchrotron radiation. Each powder sample was carefully mixed with Al_2O_3 standard powder and loaded into a 0.5 mm boron capillary. Data collection was performed at the MCX beamline of Elettra Sincrotrone Trieste using a 4-circle Huber diffractometer, equipped with a high-count-rate fast scintillation detector positioned behind a pair of slits with vertical apertures of 200 and 300 μm. A fixed wavelength of 0.8263 Å was used. Diffraction patterns were recorded while spinning the capillary in the beam, over a 2θ range from 2° to 40°, with a step size of 0.02° and a counting time of 1 s per step.

For the quantitative phase analysis, the Rietveld method was applied, and data fitting was performed using the EXPGUI interface of the GSAS software package [26]. The starting structural model for the USY framework was taken from Parise et al. and subsequently refined during the Rietveld analysis [29]. The observed and calculated profiles are reported in Figs. S1–S5 for Fe-impregnated and thermal-treated samples.

Optical characterization was carried out using a Varian Cary 5000 UV–Vis spectrophotometer equipped with a diffuse reflectance (DR) integrating sphere, operating in the 200–800 nm range. The absorption spectra were processed using the Kubelka–Munk function, $F(R_\infty)$. The optical band gap (Eg) was estimated using the Tauc approach, based on the relation $(F(R)_\infty h\nu)^\gamma = f(h\nu)$, where γ is 1/2 for indirect transitions.

To characterize the textural properties of the materials, nitrogen adsorption/desorption isotherms were obtained at −196 °C using a Micrometrics ASAP 2020Plus apparatus. Before these measurements, samples underwent a 3-hour outgassing step at 250 °C to eliminate adsorbed water and atmospheric impurities. Due to the predominantly microporous structure of the zeolites, the Langmuir method was employed to determine the specific surface area. To facilitate a comparison with the BET surface area values provided by the supplier, Tosoh Europe B.V. ($550\ m^2\ g^{-1}$ and $630\ m^2\ g^{-1}$ for the HSZ-360HUA and HSZ-390HUA zeolites, respectively), BET surface area values are also provided. The total pore volume (Vp) was derived from the nitrogen desorption isotherm at a relative pressure (P/P_0) of 0.98. The micropore volume (V_{mp}) and external surface area (S_{ext}) were determined via the t-plot method, and the pore size distribution was analyzed using the Tarazona Non-local Density Functional Theory (NL-DFT) model.

2.5. *Band structure estimation*

The edge potentials of the VB and CB of Fe_3O_4 in the optimal photocatalyst at pH = 4 were estimated using Mulliken's electronegativity theory in combination with the Nernst relationship. According to this approach, the VB edge potential (E_{VB}) and CB edge potential (E_{CB}) can be calculated as follows [30]:

$$E_{VB} = \chi - E_c + \frac{1}{2} E_{bg} - 0.059 \times \text{pH} \tag{1}$$

$$E_{CB} = E_{VB} - E_{bg} \tag{2}$$

where χ represents the absolute electronegativity of Fe_3O_4 (5.78 eV [31]), $E_c \sim 4.5$ eV denotes the energy of free electrons relative to the normal hydrogen electrode (NHE), and E_{bg} is the band gap energy of Fe_3O_4 in the optimal sample (vide infra).

2.6. *Photo-Fenton activity tests*

The photo-Fenton activity was assessed in a cylindrical batch reactor with an internal diameter of 2.6 cm, a total length of 41 cm, and a working volume of 200 mL. The reaction setup (Fig. 1) included: (i) a nitrogen distribution system delivering a flow rate of 142 Ncc min^{-1}; (ii) a peristaltic pump (Watson Marlow) to continuously recirculate the suspension and prevent catalyst sedimentation; (iii) four solar-simulating lamps symmetrically arranged around the reactor at a distance of approximately 30 mm to ensure uniform irradiation of the reaction medium; (iv) a continuous CO-CO_2 analyzer (Uras 14, ABB).

The photocatalytic tests were conducted using 100 mL of an aqueous chloramphenicol solution (initial concentration: 25 mg L^{-1}). The catalyst dosage in the reactor was varied in the range of 0.75–6 g L^{-1}. Photo-Fenton experiments were conducted using four SUN-GLO lamps (8 W each), with an emission wavelength range of 350–700 nm. The corresponding spectrum, reported in Fig. S6 (Supporting Information), shows substantial overlap with the solar spectrum in the UV–visible range. The irradiance at the external surface of the reactor was measured using a spectroradiometer (StellarNet Inc.) and was 24 mW cm^{-2}.

Hydrogen peroxide (H_2O_2) was added in concentrations ranging from 0.06 to 0.24 g L^{-1}, with the lower value representing the stoichiometric amount required for complete mineralization of the contaminant, according to the following reaction (Eq. (3)):

$$C_{11}H_{12}Cl_2N_2O_5 + 23\ H_2O_2 \longrightarrow 11\ CO_2 + 26\ H_2O + 2\ Cl^- + NH_4{}^+ + NO_3{}^- + 2H^+ \tag{3}$$

To investigate the influence of inorganic species on the degradation process, tests were performed using both distilled water and tap water as solvents. The physicochemical characteristics of the tap water are reported in Table 1.

At the start of each experiment, the reactor was filled with the aqueous solution containing CAP only. The system was then purged with nitrogen gas at ambient temperature for 10 min to establish an inert atmosphere. After this step, the catalyst was added, and the suspension

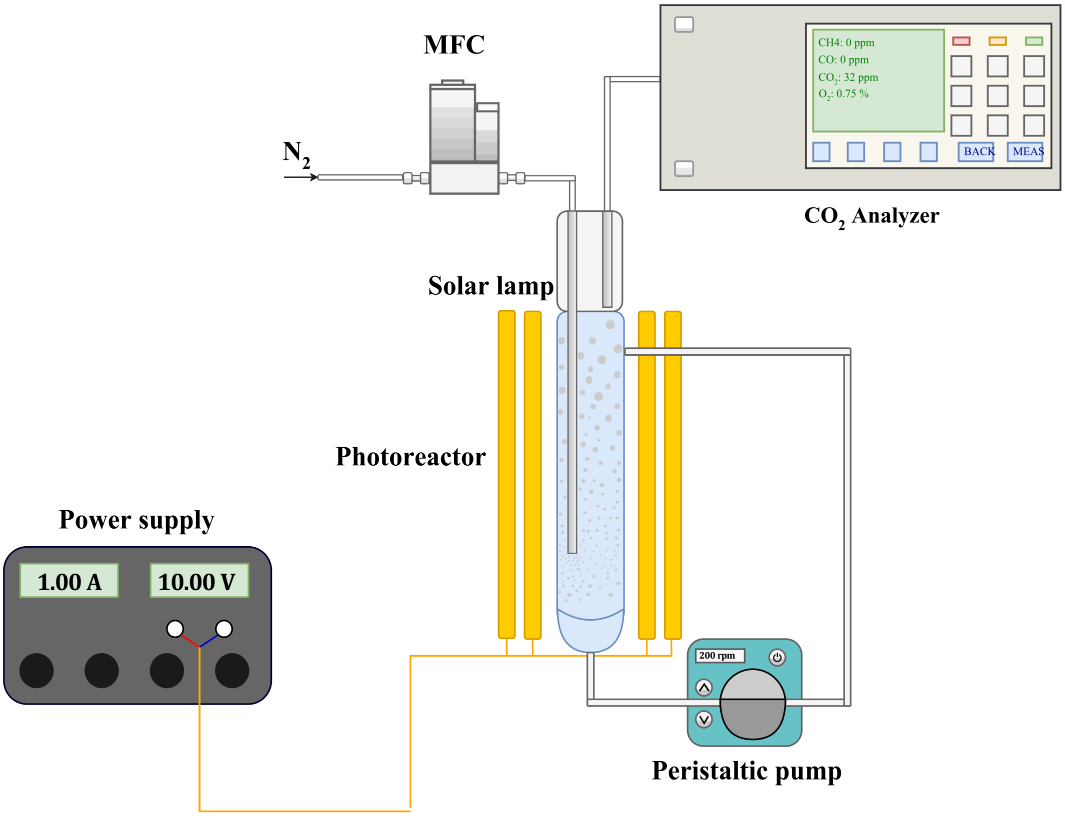

Fig. 1. Experimental setup scheme used for the photo-Fenton activity tests.

Table 1
List of the physical-chemical properties of tap water.

Property	Value
pH	7.55
Conductivity (μS cm^{-1})	468
Sodium (mg L^{-1})	3.21
Potassium (mg L^{-1})	1.2
Calcium (mg L^{-1})	85.2
Magnesium (mg L^{-1})	14
Chlorides, Cl^- (mg L^{-1})	4.7
Sulfates, SO_4^{2-} (mg L^{-1})	17.1
Bicarbonates, HCO_3^- (mg L^{-1})	314
Nitrates, NO_3^- (mg L^{-1})	3.5

was maintained under dark conditions for 30 min. This setup ensured that the observed degradation in the dark phase was not influenced by hydroxyl radical formation, allowing the role of Fe^0-induced reductive processes to be independently evaluated.

Subsequently, H_2O_2 was added, and the solar lamps were switched on to initiate the photo-Fenton reaction. After 60 min of irradiation, an additional dose of H_2O_2 at the same concentration was introduced into the reactor.

Aliquots of 3 mL were periodically withdrawn from the liquid phase for analysis. The concentration of CO_2 in the gas phase was continuously monitored at the reactor outlet using an online gas analyzer. The total organic carbon (TOC) was estimated over time based on the CO_2 concentration in the effluent gas stream measured by the continuous CO-CO_2 analyzer. The reactor was operated under atmospheric pressure (1 atm) throughout the experiments. All tests were conducted under a continuous flow of nitrogen to maintain controlled anaerobic conditions and limit the formation of oxygen-derived radicals such as superoxide. This approach was chosen to isolate the contribution of hydroxyl radicals (•OH) generated through classical photo-Fenton mechanisms, which are considered the dominant oxidative species.

Residual H_2O_2 concentrations in the liquid phase were quantified using a UV–Vis spectrophotometer (Lambda 35, PerkinElmer), by monitoring the absorbance of the H_2O_2-$TiOSO_4$ complex at 410 nm, following the method described by Eisenberg [32]. The iron content in the aqueous phase was analyzed by inductively coupled plasma spectrometry (ICP-OES, Thermo Fisher) to assess its possible leaching.

3. Results and discussion

3.1. Chemical composition

FeUSY390–500C-2 h sample was previously used by us in the mineralization of phenol, obtaining very good results [26]. We prepared the same FeUSY390–500C-2 h sample of the previous work, following a slightly different impregnation procedure, which turned out more reliable and repeatable. All the other operations performed in the preparation of this sample were the same as in the previous work [26]. FeUSY360-500C-2 h and FeUSY390–450C-2 h samples were prepared following the same impregnation procedure as the FeUSY390–500C-2 h sample, to load therein the same amount of iron.

The first step of the preparation of FeUSY360-500C-2 h, FeUSY390–450C-2 h, and FeUSY390–500C-2 h samples is the impregnation of USY360 and USY390 zeolites, in order to obtain the $FeSO_4{\cdot}7H_2O$ impregnated FeUSY360 and FeUSY390 samples. The chemical analysis of these last two samples revealed that their total Fe content is 7.2 and 7.5 wt% %, respectively. These values are in good agreement with the Fe content of the Fe-USY390 sample of our previous work [26].

3.2. Structural and textural characterization

Fig. 2 presents the X-ray diffraction (XRD) patterns of the as-received USY390 and USY360 zeolites, as well as the FeUSY samples prepared

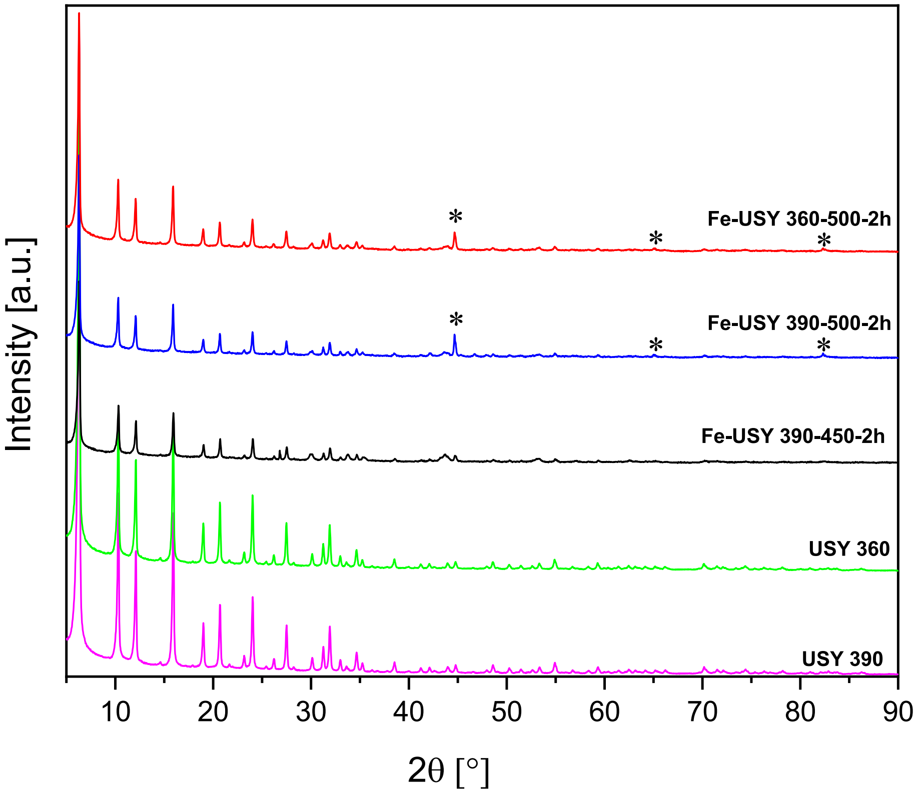

Fig. 2. XRD patterns collected on laboratory instrument of pristine USY 360 and USY 390, Fe-USY 360-500-2 h, Fe-USY 390-500-2 h, and Fe-USY 390-450-2 h. The labels identify the main peaks of α-Fe phase (*).

under different conditions: FeUSY360-500-2 h, Fe-USY390-500-2 h, and FeUSY390–450-2 h. These initial XRD data were acquired using a laboratory-based instrument as a preliminary assessment of the crystalline phases present in the materials. The diffraction patterns of the pristine USY 390 and USY 360 zeolites exhibit a high degree of similarity and are consistent with those of an ultrastable Y zeolite. The iron impregnated and thermally treated zeolite samples largely retain the profile of the parent zeolites. However, in the Fe-USY 360-500-2 h and Fe-USY 390-500-2 h samples, a distinct peak is observed at $2\theta = 44.2^\circ$, corresponding to the (110) reflection (100 % intensity) of the α-Fe phase (JCPDS card no. 06-0696). Conversely, in the Fe-USY 390-450-2 h sample, the α-Fe peak is slightly shifted, overlapping with the reflection at $2\theta = 44.8^\circ$ associated with the parent zeolite. Furthermore, this sample exhibits a distinct signal at $2\theta = 35.45^\circ$, which corresponds to the (311) plane of Fe_3O_4 (JCPDS card no. 19-0629). Detailed quantitative information obtained by the Rietveld Method is reported in Table 2.

The results of QPA clearly indicate that both the pristine zeolites contain a relevant amount of amorphous phase, probably deriving from the dealumination process that the commercial samples underwent. As a consequence, all the treated samples maintain a rather high value of amorphous phase, slightly decreasing after the thermal treatment, probably as a consequence of T-induced phase recrystallization.

Both the impregnated samples, along with the pristine zeolite and the amorphous phase, show the presence of hydrated iron sulfates containing both Fe^{2+}(Melanterite: $FeSO_4{\cdot}7H_2O$, Rozenite: $FeSO_4{\cdot}4H_2O$; and Fe^{3+} (Ferricopiapite: $Fe^{3+}{}_4(SO_4)_6(OH)_2{\cdot}20H_2O$, Butlerite: $Fe^{3+}SO_4(OH){\cdot}2H_2O$)), with ferric species as dominant in the Fe-USY (390) sample.

The intensity ratios of the low-angle peaks of the USY zeolites do not change after the impregnation process, indicating that Fe does not enter the cavities of the zeolites after the treatment, as expected from the silicatic nature of the zeolite (Fig. 3).

After the thermal treatment, all the sulfate phases transform in magnetite (Fe_3O_4), iron sulfate Pirrottine ($Fe_{1-x}S$), and, only for the sample treated at 500 °C, into Fe^0.

Fe_3O_4, which is formed by Fe^{2+}, Fe^{3+} (molar ratio 1:2) and O^{2-} ions, appears in all three of the prepared catalysts, although Ar was bubbled during the impregnation procedure, to avoid Fe^{2+} oxidation to Fe^{3+}. However, such oxidation most likely occurred during the impregnation procedure, with a greater extent observed in the USY-390 zeolite, as

Table 2
Results of quantitative phase analyses (wt% %). The number in parentheses represents the error on the last significant digit.

Phases	USY360	USY390	FeUSY 390	FeUSY 360	FeUSY 360-500-2 h	FeUSY 390-450-2 h	FeUSY 390-500-2 h
USY	55.4 (2.3)	57.9 (2.5)	23.5 (0.5)	24.2 (0.5)	44.6 (1.8)	46.8 (1.9)	51.6 (1.7)
Melanterite	–	–	16.2 (0.5)	20.4 (0.5)		–	–
Rozenite	–	–	2.3 (0.3)	3.1 (0.4)		–	–
Ferricopiapite	–	–	1.7 (0.4)	–		–	–
Butlerite	–	–	7.9 (0.3)	–		–	–
Magnetite	–	–	–	–	1.6(0.2)	9.7 (0.5)	5.6 (0.3)
Pyrrhotite	–	–	–	–	4.4 (0.3)	3.6 (0.3)	4.4 (0.3)
Fe^0	–	–	–	–	3.3 (0.3)	–	1.4 (0.1)
Amorphous	44.6 (2.3)	42.1 (2.5)	48.3 (0.9)	52.3 (0.8)	46.1 (0.8)	39.8 (1.9)	37.0 (1.8)

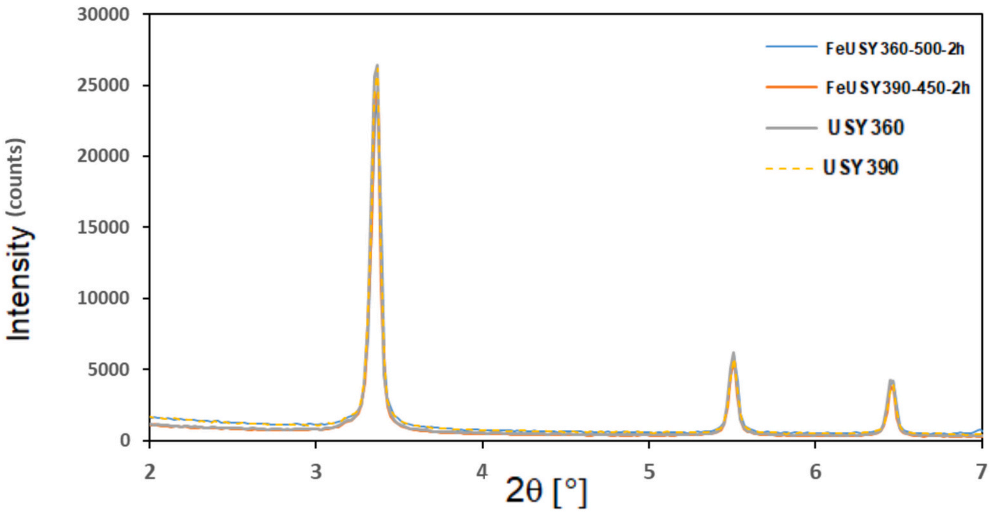

Fig. 3. XRD patterns collected on MCX instrument on USY 360 and USY 390, Fe-USY 360- and Fe-USY 390-showing that the intensity ratio of the peak does not change after the impregnation.

indicated by the higher concentration of Fe (III) sulfates (Table 2).

The amount of magnetite is higher in the FeUSY390–450C-2 h sample (9.7 vs 1.6 and 5.7 wt% % for FeUSY360–500C-2 h and FeUSY390–500C-2 h samples, respectively), which is the only sample in which Fe^0 did not crystallize.

This finding may be easily explained by the lower reduction temperature of this sample (450 °C) with respect to the others (500 °C), which results in the lower extent to which iron cations are reduced. In particular, 450 °C, as a reduction temperature, does not allow to obtain metallic iron.

As far as the samples reduced at higher temperature (500 °C, FeUSY360–500C-2 h and FeUSY390–500C-2 h) are concerned, the FeUSY360–500C-2 h sample contains a higher amount of metallic iron (Fe^0) compared to FeUSY390–500C-2 h. The authors sought plausible explanations for this observation by evaluating: (i) the porosity of the zeolite samples (vide infra); and (ii) their different shrinkage behavior upon heating [33]. Regarding porosity, the measured differences between the two samples are minimal (vide infra). Furthermore, the FeUSY390–500C-2 h sample, which contains less Fe^0, actually exhibits slightly higher mesopore and total pore volumes, a feature that would generally be expected to favor higher reducibility by means of molecular hydrogen compared to the FeUSY360–500C-2 h sample, as highlighted in a recent review on the role of mesoporous zeolites in catalytic reactions [34].

Additionally, since the FeUSY390–500C-2 h sample has a higher Si/Al ratio and thus a lower hydrophilicity and water content, it is expected to undergo less shrinkage than the FeUSY360–500C-2 h sample [33]. This different extent of contraction should affect the reducibility of Fe species in FeUSY390–500C-2 h. However, this is not observed experimentally, suggesting that other factors play a more dominant role in determining the final iron speciation. The higher Fe^0 content observed in FeUSY360–500C-2 h compared to FeUSY390–500C-2 h appears to reflect differences already present after the impregnation step, where FeUSY360 shows a greater proportion of Fe^{2+} phases.

When an Al atom is incorporated into the zeolite's silicon-oxygen framework, it creates a localised negative charge. To balance this charge, a proton attaches nearby, forming a Brønsted acid site.

When there's a lower Si/Al ratio, it means a higher concentration of Al atoms in the zeolite structure, which directly translates to a higher overall number or density of Brønsted acid sites [35].

Conversely, a higher Si/Al ratio means increased strength of individual acid sites (more isolated strong Brønsted sites). The different Si/Al ratios of FeUSY360 and FeUSY390, and consequently their different acidity and density of Brønsted sites, seem to influence the strength of the interactions between the positively charged cations and the negatively charged zeolite structure. As a consequence, there is a different degree of oxidation of Fe^{2+} to Fe^{3+} in the impregnated zeolites as a function of the Si/Al ratio, which probably affects the reducibility to Fe^0 of the final catalyst.

It is worth noting that most literature data on zeolite acidity refer to ion-exchanged and calcined materials, studies specifically addressing acidity and metal–zeolite interactions [27,36,37]. Overall, it remains challenging to unambiguously identify which specific factors govern the nature of the iron-containing phases, as their formation appears to result from the combined influence of multiple interdependent properties of the zeolite system.

UV–Vis spectroscopy was used to investigate the optical absorption properties of the samples after iron incorporation and thermal treatment. The pristine zeolites (USY 360 and USY 390) showed no significant absorption in the examined spectral range, indicating their optical inactivity. In contrast, the Fe-containing samples exhibited distinct absorption bands at approximately 210 nm and 276 nm attributed to O^{2-}/Fe^{3+} ligand to metal charge transfer transitions, as shown in Fig. S7a [38]. The intensity of these bands increased with the Fe_3O_4 content in the zeolite samples, suggesting that Fe_3O_4 plays a key role in enhancing the photoactivity of the materials. Additionally, a broader absorption feature centered around 480 nm was observed only in the samples FeUSY390–500C-2 h and FeUSY390–450C-2 h, which can be attributed to d–d charge transfer transitions involving the transition of octahedrally coordinated Fe^{3+}, in agreement with literature reports [39,40]. The band gap energies, calculated from Tauc's plots assuming an indirect transition (Fig. S7b), are in the range of 2.27–2.40 eV, consistent with literature values for materials containing Fe_3O_4 [41].

The textural properties of the FeUSY catalysts were investigated using nitrogen adsorption-desorption at 77 K, with the resulting isotherms presented in Fig. 4. The isotherms for all FeUSY samples display a similar composite nature, exhibiting a steep initial uptake at low relative pressures ($P/P_0 < 0.05$), indicative of micropore filling (width ≤1 nm), characteristic of Type I isotherms. Conversely, the presence of a Type H4 hysteresis loop supports the presence of additional porosity in the range of mesopores. At higher relative pressures ($P/P_0 > 0.4$), the isotherms show an upward convexity, consistent with Type II behavior and suggesting the presence of larger mesopores or a degree of macroporosity. The presence of these secondary mesopores, alongside the preserved microporous framework in all thermally treated samples, supports the classification of the prepared catalysts as exhibiting a hierarchical

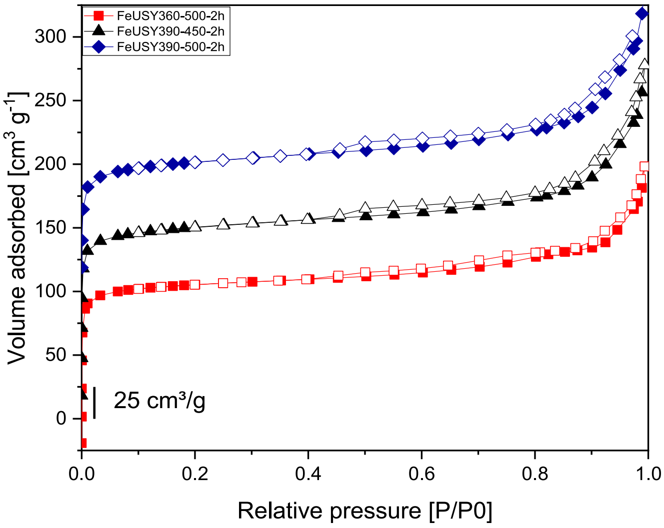

Fig. 4. N_2 adsorption/desorption isotherms at 77 K of FeUSY360–500-2 h, FeUSY390–500-2 h, and FeUSY390–450-2 h samples. Adsorption and desorption branches were indicated with filled and empty symbols, respectively. For the sake of clarity, the curves were shifted.

porous architecture [42].

A detailed porosity analysis was carried out using the NL-DFT method with the Tarazona kernel model. The pore size distributions are shown in Fig. 5a and clearly highlight the presence of the characteristic pore (commonly referred to as the "supercage") of these ultrastable Y zeolites, centered around an average diameter of approximately 0.9 nm. Only minimal differences can be observed between the two types of zeolites. The maximum of the pore size distribution is consistent with the porosity value reported by the manufacturer (Tosoh Europe B.V.) for the parent zeolites, USY360 and USY390, indicating that neither the iron ion exchange process nor the subsequent thermal treatment significantly altered the porous framework of the starting materials.

Although the majority of the pore volume is located in the microporous region, the presence of small mesopores is evidenced by a minor peak at approximately 1.3 nm. The cumulative pore volume curve, presented in Fig. 5b, further reveals the existence of an additional porous fraction, attributed to larger mesopores, most likely formed during the dealumination process. This multiscale porosity results in a hierarchical structure, which may provide significant advantages in terms of molecular accessibility and diffusion of reactants [42–44].

For materials exhibiting mixed porosity, selecting an appropriate and robust method to determine specific surface area remains a significant challenge [45]. Accordingly, both Langmuir and BET surface area values are reported in Table 3. Notably, the BET analysis yields a negative intercept and a low C constant, indicating limitations of this model for the present systems [46].

Despite these limitations, BET values are included to facilitate direct comparison with manufacturer-provided data (550 m^2 g^{-1} for USY360 and 630 m^2 g^{-1} forUSY 390) and to assess the impact of iron ion exchange and thermal treatment on the porous structure. As shown in Table 3, all modified samples exhibit lower specific surface areas than their parent zeolites, implying a slight yet measurable alteration of the original framework. Among them, FeUSY360–500-2 h presents the lowest BET and Langmuir specific surface areas.

Given the composite nature of the isotherms (type I + type II), indicative of substantial external surface contributions alongside microporosity, external surface areas were also calculated using the t-plot method. These values, reported in Table 3, follow a trend consistent with the total surface areas, with FeUSY390–500-2 h showing the highest external surface. Moreover, a greater mesoporous volume fraction is observed in samples derived from USY390, suggesting enhanced structural reorganization during treatment.

3.3. Catalytic tests

3.3.1. Catalytic performance of Fe^0/Fe_3O_4/USY composites in solar photo-Fenton chloramphenicol degradation

To better highlight the contribution of metallic iron and magnetite to

Table 3
Textural properties, including specific surface area (BET and Langmuir), external surface area (S_{ext}), micropore volume (V_{mp}) and total pore volume (V_p).

Sample	$S_{Langmuir}$	S_{BET}	t-plot		
			S_{ext}	V_{mp}	V_p
	(m^2 g^{-1})	(m^2 g^{-1})	(m^2 g^{-1})	(cm^{3}g^{-1})	(cm^{3}g^{-1})
FeUSY360–500-2 h	631	[a]441	92	0.18	0.25
FeUSY390–450-2 h	653	[a]482	120	0.18	0.36
FeUSY390–500-2 h	700	[a]484	126	0.20	0.40

[a] Range 0.12–0.25 P/P_0, C_{BET} negative, value not acceptable, S_{ext} range 0.3–0.4 nm thickness.

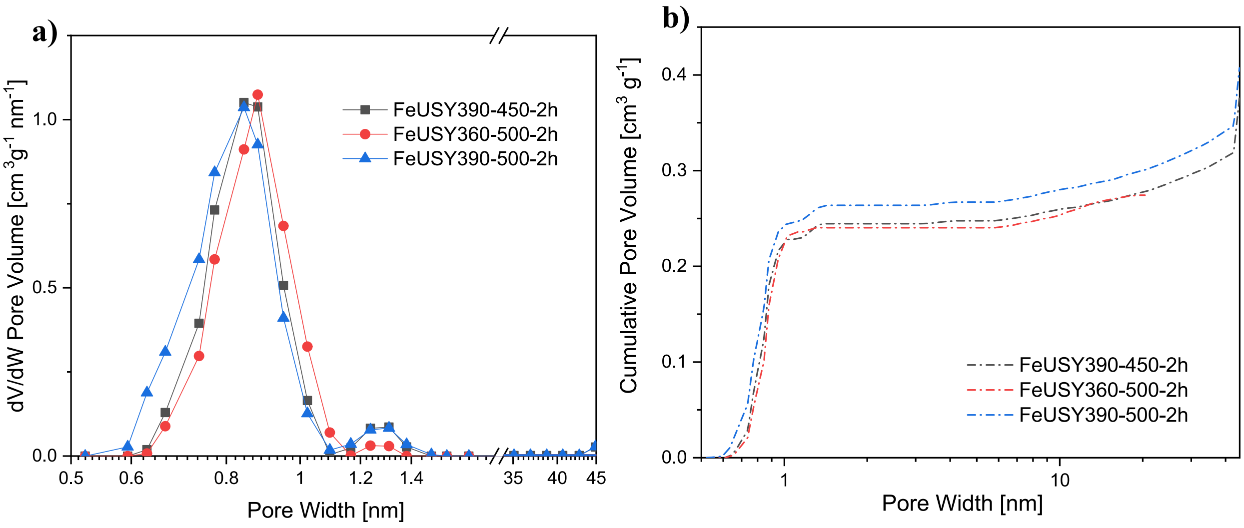

Fig. 5. a) Pore size distribution and b) cumulative pore volume of FeUSY360–500-2 h, FeUSY390–500-2 h, and FeUSY390–450-2 h samples.

the catalytic response, we decided to name the samples in this section of the work based on the weight percentages of Fe^0 and Fe_3O_4 obtained from QPA. Henceforth, FeUSY390–450-2 h will be referred to as Fe_3O_4(9.7 %)/USY390, FeUSY390–500-2 h as Fe^0(1.4 %)/Fe_3O_4(5.6 %)/USY390, and FeUSY360–500-2 h as Fe^0(3.3 %)/Fe_3O_4(1.6 %)/USY360. Initially, the influence of zero-valent iron (Fe^0) and magnetite (Fe_3O_4) incorporated into the Fe^0/Fe_3O_4/USY catalysts was systematically assessed in the solar photo-Fenton degradation of CAP. The experiments were carried out under acidic conditions (pH = 4) [26], using a constant catalyst dosage of 3 g L^{-1} and a stoichiometric amount of hydrogen peroxide (H_2O_2, 0.06 g L^{-1}). The goal of this preliminary screening was to evaluate the individual and synergistic roles of Fe^0 and Fe_3O_4 in CAP removal, both in the absence of light (dark phase) and under simulated solar irradiation. The resulting CAP degradation profiles are presented in Fig. 6.

During the dark phase, a marked initial decrease in CAP concentration is observed only in the presence of Fe^0-containing catalysts. Notably, Fe^0(3.3 %)/Fe_3O_4(1.6 %)/USY 360 leads to a drastic drop in c/c_0 (~0.08 within 5 min), indicating a significant reductive transformation of CAP even in the absence of light. This effect is attributed to the generation of hydrogen radicals (H•) via Fe^0 oxidation.

$$Fe^0 + 2H^+ \rightarrow Fe^{2+} + 2H \tag{4}$$

$$C_{11}H_{12}Cl_2N_2O_5 + H^{\bullet} \rightarrow \text{intermediates} \tag{5}$$

Although hydrogen radicals were not directly detected in this study, their formation is mechanistically plausible based on the established reactivity of Fe^0 with protons under acidic conditions. In particular, Fe^0 can react with H^+ to generate Fe^{2+} and H• species (Eq. (4)), which are known to initiate reductive dehalogenation of chlorinated organic molecules [47]. Similar degradation pathways have been proposed in other advanced reduction processes for CAP, where H• contributed to the cleavage of C—Cl bonds [48,49] (Eq. (5)). However, it is also possible that surface-adsorbed hydrogen or direct electron transfer mechanisms contribute to the reductive degradation of CAP [50–52].

A less pronounced yet evident activity is also seen for Fe^0(1.4 %)/Fe_3O_4(5.6 %)/USY 390 and, to a smaller extent, for Fe_3O_4(9.7 %)/USY 390.

Conversely, the USY 390 and USY 360 zeolites showed a moderate decrease in CAP concentration, with c/c_0 reaching ~0.9 and ~0.6, respectively. This behavior is mainly attributed to physisorption of CAP onto the high surface area and porous structure of the zeolite frameworks. The greater removal observed with USY 360 may be related to the enhanced surface acidity, which could increase CAP-zeolite interactions in the absence of redox-active sites.

Upon exposure to solar irradiation, Fe^0(3.3 %)/Fe_3O_4(1.6 %)/USY 360 exhibited the highest degradation performance, achieving almost complete removal ($c/c_0 < 0.01$) after 150 min.

Catalysts with lower Fe^0 content displayed moderate activity, with final c/c_0 values around 0.2 for Fe^0(1.4 %)/Fe_3O_4(5.6 %)/USY 390 and 0.30 for Fe_3O_4(9.7 %)/USY 390. The system containing only H_2O_2 showed a CAP degradation performance lower than Fe-containing catalysts, confirming that iron species are indispensable for efficient photo-Fenton-based oxidation. This observation aligns with the negligible CAP removal observed in the photolysis control test (CAP + light only; data not shown), confirming that neither direct photolysis nor the activation of H_2O_2 in the absence of Fe-containing catalysts is sufficient for significant pollutant degradation. It is worth noting that the slight degradation observed for USY360 and USY390 samples under irradiation can be attributed to the photo-assisted activation of H_2O_2, rather than any catalytic activity of the zeolite supports. This behavior is confirmed by control tests carried out with H_2O_2 only, which showed comparable CAP degradation levels.

Overall, these results clearly demonstrate that the presence and proportion of Fe^0 significantly influence CAP degradation, especially in the early (dark) stage, while both Fe^0 and Fe_3O_4 contribute to sustained catalytic performance under simulated solar light.

Fig. 7 further elucidates the impact of Fe^0 loading on both CAP degradation efficiency and mineralization performance. Fig. 7a presents the degradation efficiency after 30 min of dark-phase treatment, confirming that Fe^0 plays a crucial role in initiating CAP removal even in the absence of light. An increasing Fe^0 content correlates with higher degradation, with Fe^0(3.3 %)/Fe_3O_4(1.6 %)/USY 360 achieving ~98.4 % CAP removal, compared to 75.3 % and 61.5 % for Fe^0(1.4 %)/Fe_3O_4(5.6 %)/USY 390 and Fe_3O_4(9.7 %)/USY 390, respectively.

To better evaluate the influence of Fe^0 content on catalytic performance, the specific contribution of zero-valent iron was isolated by subtracting the activity of the Fe^0-free sample (Fe_3O_4(9.7 %)/USY 390, 61.5 % degradation) from that of the Fe^0-containing systems. The addition of 1.4 wt% Fe^0 resulted in a net degradation improvement of 13.8 %, while 3.3 wt% Fe^0 led to a 36.9 % enhancement. This corresponds to a 2.67-fold increase in degradation efficiency relative to a 2.36-fold increase in Fe^0 content. The near-proportional relationship strongly suggests that Fe^0 species are well-dispersed and catalytically accessible. If Fe^0 particles were significantly agglomerated, a plateau or even a decline in degradation efficiency would likely occur at higher loadings due to limited surface accessibility. These findings provide indirect yet compelling evidence of effective Fe^0 dispersion across the zeolitic surface.

These data further support the role of Fe^0 on CAP degradation during

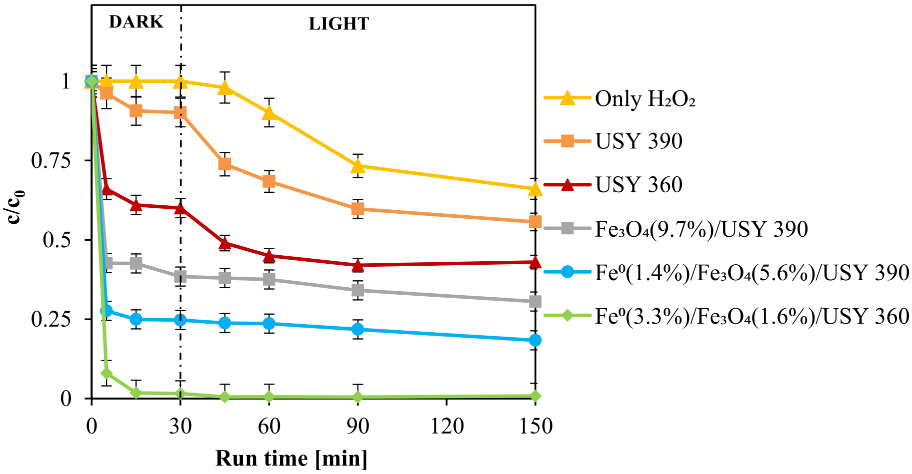

Fig. 6. CAP relative concentration (c/c_0) as a function of run time during the dark and irradiation time. Experimental conditions: $[CAP]_0 = 25$ ppm, $[H_2O_2] = 0.06$ g L^{-1}, pH = 4, catalyst dosage = 3 g L^{-1}.

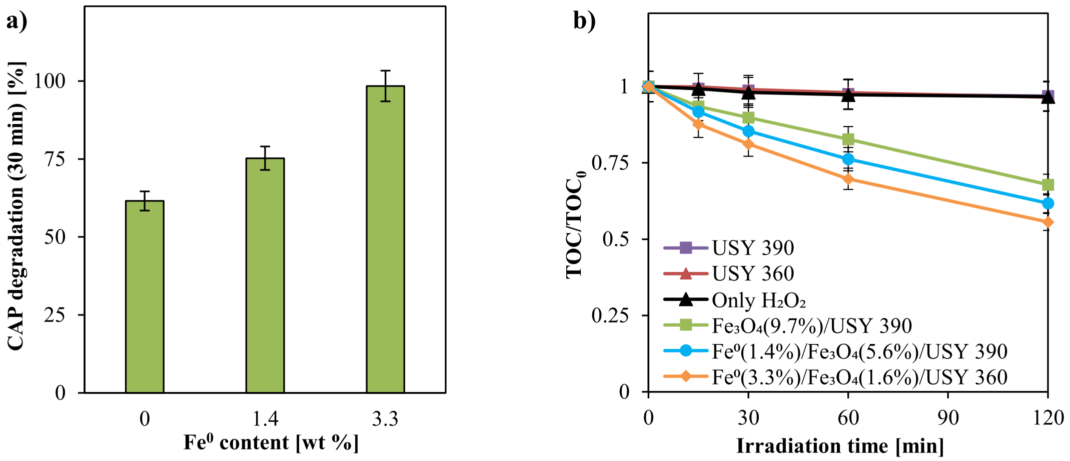

Fig. 7. (a) CAP degradation efficiency (%) after 30 min of dark-phase treatment; (b) CAP mineralization profiles expressed as TOC/TOC_0 versus irradiation time under solar light using Fe^0/Fe_3O_4/USY catalysts. Experimental conditions: $[CAP]_0 = 25$ ppm, $[H_2O_2] = 0.06$ g L^{-1}, pH = 4, catalyst dosage = 3 g L^{-1}.

the dark phase [26,49].

TOC analysis after 120 min of solar light irradiation (Fig. 7b) evidenced that Fe^0(3.3 %)/Fe_3O_4(1.6 %)/USY 360 exhibited the highest mineralization activity, achieving a TOC removal of about 45 %, compared to 38 % for Fe^0(1.4 %)/Fe_3O_4(5.6 %)/USY 390 and 32 % for Fe_3O_4(9.7 %)/USY 390. These values indicate that while Fe^0 is essential for initiating the process, the combination with Fe_3O_4 enhances long-term mineralization efficiency through redox cycling and sustained generation of reactive oxygen species.

To verify the consumption of hydrogen peroxide during the photo-Fenton process, its concentration was measured at the end of the illumination phase. The analysis revealed complete depletion of H_2O_2, confirming its active participation in the reaction.

Control experiments using H_2O_2 alone and USY 360 and USY 390 zeolites in the presence of H_2O_2 under irradiation resulted in negligible CAP mineralization (~3 %) after 120 min of irradiation (Fig. 7b), emphasizing the critical role of iron-based active sites in facilitating oxidative degradation.

Indeed, in the light phase, the activation of H_2O_2 in the presence of iron species generated hydroxyl radicals ($\cdot OH$) through the photo-Fenton mechanism, facilitating the oxidative degradation of CAP intermediates and enhancing overall mineralization. Fe_3O_4 played a pivotal role in sustaining the reaction by enabling continuous Fe^{3+}/Fe^{2+} redox cycling under irradiation. Acting as an electron mediator, Fe_3O_4 promoted the reduction of Fe^{3+} to Fe^{2+}, which subsequently reacted with H_2O_2 to generate $\cdot OH$ via the Fenton reaction ($Fe^{2+} + H_2O_2 \rightarrow Fe^{3+} + \cdot OH + OH^-$) [53,54]. This process ensured a continuous production of ROS during the light phase, facilitating the mineralization of CAP intermediates.

In summary, these results highlight the synergistic contribution of Fe^0, Fe_3O_4, and the USY zeolite. While Fe^0 promotes reductive degradation in the dark and supplies Fe^{2+} ions, Fe_3O_4 enables photoreduction of Fe^{3+} under irradiation, sustaining $\cdot OH$ production. The USY support enhances the dispersion of active phases and promotes the adsorption of CAP, ensuring efficient proximity between reactants and catalytic sites. This combined action results in superior degradation and mineralization performance compared to binary or single-component systems.

Subsequent experiments were conducted with the most efficient catalyst, Fe^0(3.3 %)/Fe_3O_4(1.6 %)/USY 360, to determine optimal operating conditions, assess its stability, evaluate its activity in real aqueous matrices, and elucidate the reaction mechanism driving the process.

3.3.2. *Influence of Fe^0(3.3 %)/Fe_3O_4(1.6 %)/USY 360 dosage*

The effect of catalyst dosage on the degradation and mineralization of CAP was examined under both dark and illuminated conditions (Fig. 8). Experiments were conducted in an acidic medium (pH = 4), utilizing catalyst dosages ranging from 0.75 to 4.5 g L^{-1}. The initial CAP concentration was maintained at 25 ppm, while hydrogen peroxide was introduced at a stoichiometric dosage of 0.06 g L^{-1}.

A significant enhancement in removal efficiency was observed as the catalyst concentration increased from 0.75 to 1.5 g L^{-1}. In the absence of light, the degradation efficiency at 5 min rose from 59.3 % at 0.75 g L^{-1} to 92.0 % at 1.5 g L^{-1} (Fig. 8a). Under irradiation, the mineralization efficiency at 120 min followed a similar trend, improving from 20 % to 44 % (Fig. 8b).

This improvement can be attributed to the greater availability of active sites, which promotes the generation of reactive oxygen species and enhances interactions between CAP molecules and oxidizing radicals [55–57].

However, beyond 1.5 g L^{-1}, no further enhancement was observed. At catalyst dosages of 3 and 4.5 g L^{-1}, CAP degradation efficiency remained nearly constant (91.8 % and 91.4 %, respectively) (Fig. 8a), and TOC removal slightly decreased (Fig. 8b). This decline can be attributed to excessive catalyst loading, which reduces photon penetration due to light scattering and shielding effects from suspended particles, limiting the activation of Fe_3O_4 and H_2O_2 [57,58].

Based on these results, 1.5 g L^{-1} was identified as the optimal catalyst dosage for CAP removal, balancing efficiency and photon utilization.

3.3.3. *Influence of H_2O_2 dosage*

In the photo-Fenton process, the concentration of H_2O_2 plays a critical role in the degradation and mineralization of CAP (Fig. 9), as it serves as the primary source of reactive radical species. During the dark phase, CAP degradation was largely unaffected by changes in H_2O_2 dosage, with efficiencies consistently above 98 % (Fig. 9a). This indicates that, in the absence of light, the degradation process is predominantly driven by Fe^0, and not significantly influenced by the oxidant concentration.

At an H_2O_2 dosage of 0.06 g L^{-1}, TOC removal reached approximately 45 % after 120 min of irradiation, while at 0.12 g L^{-1} it increased to about 54 %, with complete consumption of H_2O_2. In contrast, at 0.24 g L^{-1}, TOC removal declined sharply to 20 %, and approximately 40 % of the initial H_2O_2 remained unreacted even after 120 min.

This reduced efficiency and incomplete oxidant utilization suggest that excessive H_2O_2 concentrations promote self-decomposition into oxygen and water, and increase the likelihood of hydroxyl radical scavenging, forming less reactive hydroperoxide radicals, as described by Eqs. (6) and (7) [26,59].

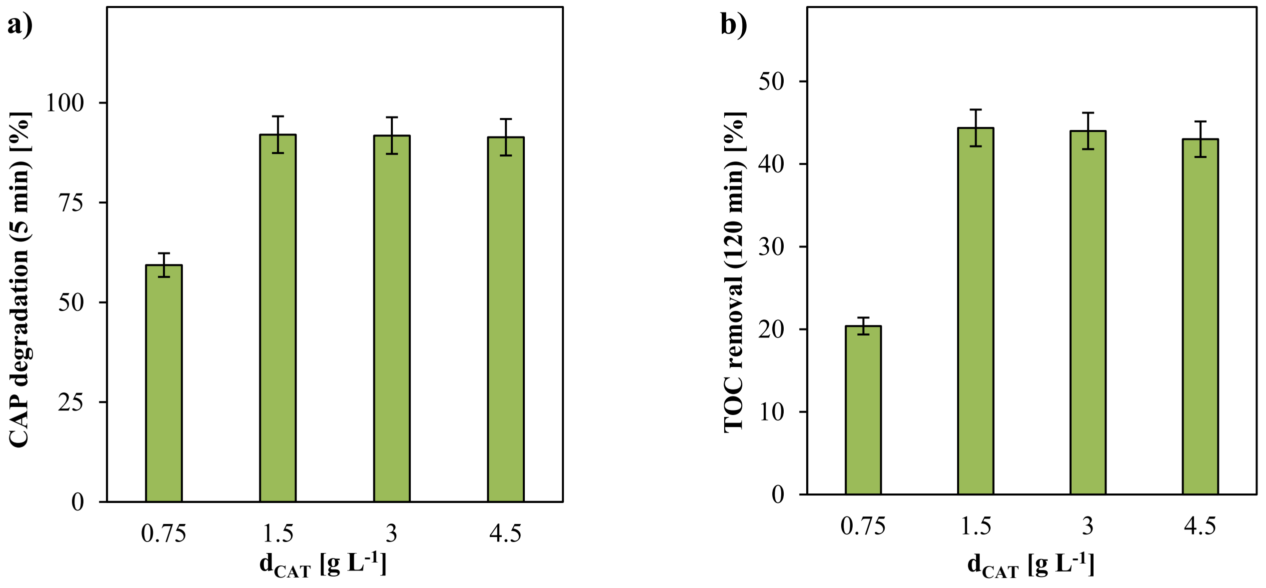

Fig. 8. (a) CAP degradation efficiency after 5 min of dark-phase treatment at different catalyst dosages (d_{CAT}); (b) TOC removal after 120 min of solar irradiation using Fe^0(3.3 %)/Fe_3O_4(1.6 %)/USY 360. Experimental conditions: $[CAP]_0 = 25$ ppm, $[H_2O_2] = 0.06$ g L^{-1}, pH = 4.

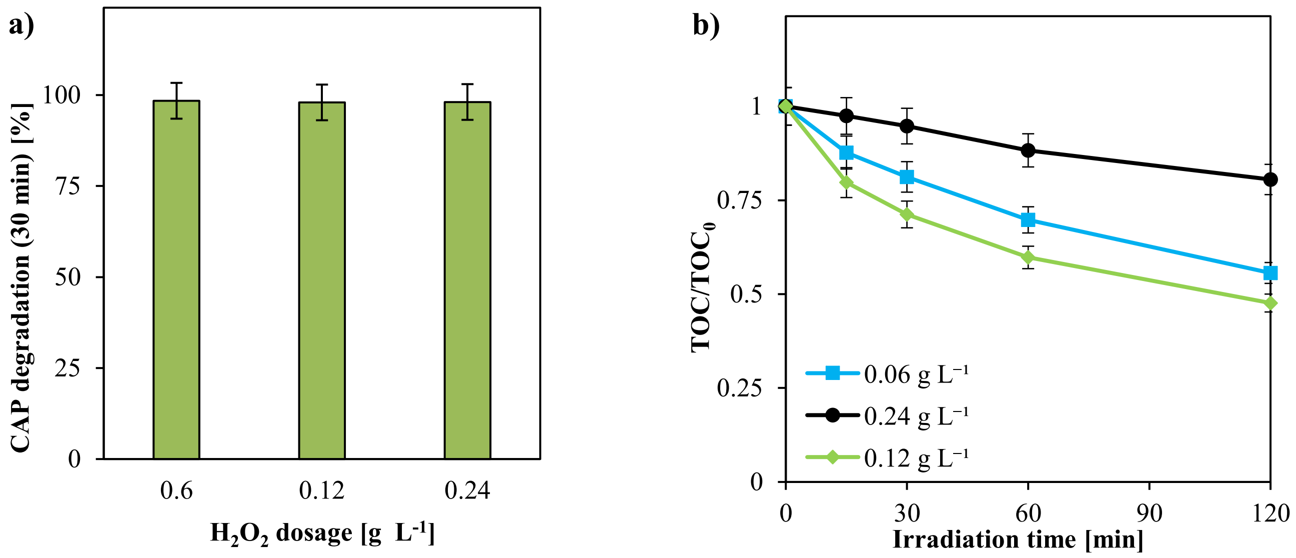

Fig. 9. (a) CAP degradation efficiency after 30 min of dark-phase treatment using Fe^0(3.3 %)/Fe_3O_4(1.6 %)/USY 360 at different H_2O_2 dosages; (b) CAP mineralization under solar irradiation (expressed as the ratio TOC/TOC$_0$, where TOC is the residual total organic carbon at time t, and TOC$_0$ is the initial value) as a function of irradiation time at different H_2O_2 dosages. Reaction conditions: $[CAP]_0 = 25$ ppm, pH = 4, catalyst dosage = 1.5 g L^{-1}.

$$2\,H_2O_2 \rightarrow 2\,H_2O + O_2 \quad (6)$$

$$OH^{\cdot} + H_2O_2 \rightarrow HO_2^{\cdot} + H_2O \quad (7)$$

These findings indicate that the optimal initial dosage of H_2O_2 for effective CAP mineralization is 0.12 g L^{-1}, which ensures complete oxidant utilization while minimizing radical scavenging effects.

3.3.4. Influence of initial pH and Fe^0(3.3 %)/Fe_3O_4(1.6 %)/USY 360 stability

The influence of initial pH on CAP degradation and mineralization efficiencies was evaluated using the Fe^0(3.3 %)/Fe_3O_4(1.6 %)/USY catalyst. In addition to the spontaneous pH (6.5), an acidic pH of 4 was selected based on our previous work, in which a similar Fe-based catalytic system was evaluated under both unadjusted and acidic conditions, and pH 4 was identified as the most effective for enhancing photo-Fenton activity [26]. As shown in Fig. 10, CAP degradation during the dark phase remained essentially unaffected by pH variations (Fig. 10a), with degradation efficiencies consistently near 100 %, confirming that the reaction in this stage is mainly governed by Fe^0-mediated reductive processes.

However, during the light phase, mineralization was notably lower under spontaneous pH conditions, reaching a value of only ~29 % after 120 min of irradiation (Fig. 10b). In contrast, under acidic conditions (pH = 4), the mineralization efficiency increased significantly to ~52 %, highlighting the enhanced degradation efficiency in acidic media.

The enhanced performance at acidic pH aligns with previous studies on heterogeneous photo-Fenton processes employing iron-based catalysts, where optimal degradation efficiencies were observed under acidic conditions [26,60]. This behavior is primarily attributed to the higher oxidation potential of hydroxyl radicals in acidic media [61].

In these systems, iron species play a crucial role in the catalytic cycle:

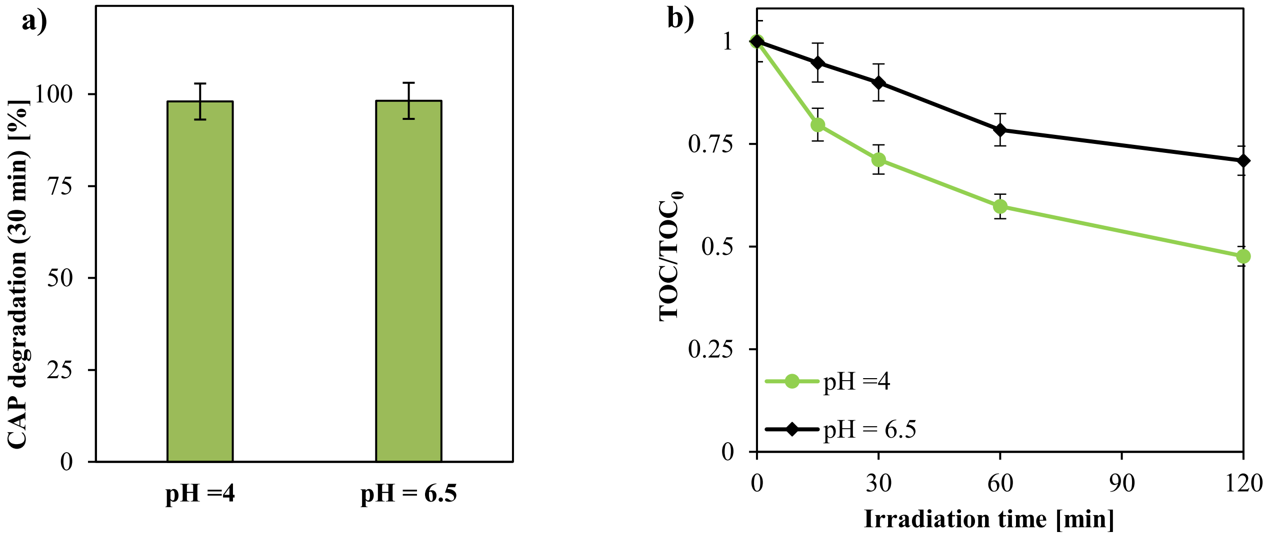

Fig. 10. (a) CAP degradation efficiency after 30 min of dark-phase treatment using Fe^0(3.3 %)/Fe_3O_4(1.6 %)/USY 360 at two initial pH values (4 and 6.5); (b) CAP mineralization under solar irradiation for 120 min (expressed as TOC/TOC₀, where TOC is the total organic carbon at time t and TOC₀ is the initial value). Experimental conditions: $[CAP]_0 = 25$ ppm, $[H_2O_2] = 0.12\ g\ L^{-1}$, catalyst dosage = 1.5 g L^{-1}.

surface-bound ferrous iron ($\equiv Fe^{2+}$) reacts with hydrogen peroxide to generate •OH, which initiates pollutant degradation (Eq. (8)). The resulting ferric species ($\equiv Fe^{3+}$) must then be reduced back to $\equiv Fe^{2+}$ to sustain the reaction cycle. This reduction can occur via two primary pathways [26,61]:

(i) reaction with hydrogen peroxide (Eq. (9)), yielding hydroperoxide radicals (HO_2•), which have lower oxidative potential than hydroxyl radicals, or (ii) photoreduction in the presence of water (Eq. (10)), leading to additional hydroxyl radical formation.

Moreover, acidic conditions limit the formation of iron hydroxide complexes, which would otherwise hinder the reduction of $\equiv Fe^{3+}$ back to $\equiv Fe^{2+}$, thus maintaining catalyst activity [26,61,62].

Conversely, at higher pH values, the disproportionation of H_2O_2 into molecular oxygen is more prevalent, reducing the availability of hydroxyl radicals and, consequently, the efficiency of the degradation process [26,61–63].

$$\equiv Fe^{2+} + H_2O_2 \rightarrow \equiv Fe^{3+} + OH^- + \dot{O}H \tag{8}$$

$$\equiv Fe^{3+} + H_2O_2 \rightarrow \equiv Fe^{2+} + H^+ + HO_2^{\cdot} \tag{9}$$

$$\equiv Fe^{3+} + H_2O + h\,\nu \rightarrow \equiv Fe^{2+} + \dot{O}H + H^+ \tag{10}$$

However, although ~98 % degradation of CAP was achieved in dark conditions, TOC removal reached a plateau at ~52 %, suggesting the accumulation of persistent oxidation intermediates. Likely, the initial reductive transformation of CAP by Fe^0 during the dark phase led to the formation of dechlorinated byproducts that are more resistant to mineralization. Upon H_2O_2 addition and light exposure, further oxidation via •OH radicals occurred, but complete mineralization was not achieved within the studied time. This behavior is consistent with previous reports showing that partially dechlorinated aromatics, nitroderivatives, or short-chain carboxylic acids formed during early-stage reduction can persist in solution [52,64] and may require prolonged oxidative treatment to be fully mineralized.

To assess the catalyst's stability, five consecutive degradation cycles were conducted under acidic conditions (pH = 4), using Fe^0(3.3 %)/Fe_3O_4(1.6 %)/USY 360. After each run, the catalyst was recovered by magnetic separation [26,65], rinsed with distilled water, and reused without any additional treatment. The mass of the recovered catalyst was measured gravimetrically at the end of each cycle. The mass loss was negligible (<2 %), indicating high mechanical stability of the catalyst during operation and recovery.

As shown in Fig. 11, the mineralization efficiency remained stable across all cycles, with an average TOC removal of 52 ± 3 % after 120 min of irradiation.

Iron content in the aqueous phase was analyzed after each reuse cycle using ICP-OES to check for potential leaching. The results confirmed that Fe was below the detection limit of the instrument (<0.01 mg L^{-1}), indicating negligible or absent leaching during the reactions.

These results confirm the excellent reusability and structural robustness of the catalyst, demonstrating consistent photocatalytic performance over multiple consecutive applications.

3.3.5. Effect of water matrix on CAP removal

For the practical application of heterogeneous photo-Fenton systems in water treatment, it is essential to evaluate how real water matrices affect photocatalytic performance, particularly in the presence of common inorganic ions such as chloride, phosphate, and nitrate. These

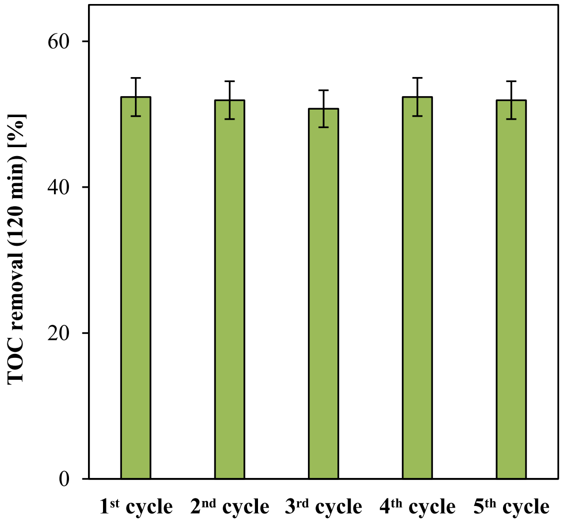

Fig. 11. Stability of Fe^0(3.3 %)/Fe_3O_4(1.6 %)/USY 360 over five consecutive cycles in CAP mineralization. TOC removal was measured after 120 min of solar irradiation. Experimental conditions: $[CAP]_0 = 25$ ppm, $[H_2O_2] = 0.12\ g\ L^{-1}$, catalyst dosage = 1.5 g L^{-1}, pH = 4.

species, typically found in surface and municipal waters, may impair oxidative processes by scavenging reactive oxygen species (e.g., hydroxyl radicals and photogenerated holes) or by competitively adsorbing onto catalyst surface sites [66–68].

To assess this influence, the Fe^0(3.3 %)/Fe_3O_4(1.6 %)/USY 360 catalyst was tested under optimal operating conditions using tap water (TW) artificially spiked with chloramphenicol (CAP), and compared with results obtained using distilled water (DW) (Fig. 12). As illustrated in Fig. 12a, CAP degradation during the dark phase remained highly effective in both water matrices, achieving ~98 % removal. This indicates that adsorption and initial CAP reduction are not significantly hindered by the presence of background ions in TW.

However, during the solar irradiation phase, a reduction in mineralization was observed in TW, despite the complete consumption of H_2O_2 in both matrices. After 120 min of irradiation, TOC removal in TW reached approximately 42 %, whereas in DW it was around 52 % (Fig. 12b). These findings indicate that, although the presence of inorganic ions does not interfere with CAP degradation in the dark, it does affect the mineralization of intermediates during the light phase. This decline in performance can be attributed to the presence of anionic species in TW, which may act as radical scavengers or compete with CAP for adsorption onto active catalytic sites.

Indeed, recent studies have demonstrated that ions such as Cl^-, NO_3^-, and PO_4^{3-} can substantially inhibit photo-Fenton reactions by reacting with hydroxyl radicals to produce less reactive species, such as Cl• and NO_3•, or by blocking or deactivating surface catalytic sites [69,70].

These observations highlight the importance of accounting for the ionic composition of the water matrix when designing and optimizing photo-Fenton systems for environmental applications such as CAP removal. Nevertheless, the Fe^0(3.3 %)/Fe_3O_4(1.6 %)/USY 360 catalyst retained a high level of activity under realistic conditions, demonstrating robustness and applicability despite the moderate decrease in mineralization efficiency due to matrix effects.

3.3.6. Role of reactive oxygen species in the solar-light-assisted CAP removal over Fe^0(3.3 %)/Fe_3O_4(1.6 %)/USY

The influence of ROS on the degradation mechanism of CAP was investigated through photo-Fenton experiments using the Fe^0(3.3 %)/Fe_3O_4(1.6 %)/USY 360 catalyst under solar light irradiation. Scavenger assays were performed under optimized reaction conditions (initial CAP concentration = 25 ppm, photocatalyst dosage = 1.5 g L^{-1}, H_2O_2 dosage = 0.06 g L^{-1}, and pH = 4) to identify the predominant oxidative species involved.

Specific probe molecules were employed to quench target ROS: isopropanol (10 mM) was used as a hydroxyl radical scavenger, consistent with previous studies [71], silver nitrate (10 mM) served to capture photogenerated electrons [26], and potassium iodide (10 mM) was utilized to capture photogenerated holes on the Fe_3O_4 surface [72]. Although IPA is not a perfectly selective scavenger, it is widely employed in advanced oxidation processes due to its high reactivity toward •OH, and is considered a reliable diagnostic tool when used at controlled concentrations. A recent study by Ding et al. [73] has shown that at IPA concentrations exceeding 20 mM, unintended side phenomena can occur, such as the in situ generation of H_2O_2 and the unexpected formation of superoxide radicals, which could lead to misattribution of oxidative species in photocatalytic systems. In our experiments, the IPA concentration was kept at 10 mM, thereby minimizing such side effects and ensuring that the observed inhibition could be predominantly attributed to the scavenging of •OH.

The selection of $AgNO_3$ is justified by its favorable redox potential (Ag^+/Ag^0, $E^0 = +0.80$ V vs. NHE), which exceeds that of Fe^{3+}/Fe^{2+} ($E^0 = +0.77$ V vs. NHE), thereby enabling preferential reduction of Ag^+ over Fe^{3+} by conduction band electrons from Fe_3O_4 [26,74]. Notably, magnetite's narrow band gap (2.2 eV [75,76]) allows visible light absorption, supporting its role in photocatalytic activation [40,75–77]. This prompted further evaluation of photocatalytic contributions by tracking ROS-mediated pathways. To assess the involvement of superoxide, additional tests were conducted under an oxygen-rich environment by aerating the reactor with air (flow rate: 142 cm^3 min^{-1} STP) instead of nitrogen. The obtained results are reported in Fig. 13, while a schematic overview of the main radical and photogenerated charge transfer pathways contributing to CAP degradation is provided in Fig. 14, and is discussed in more detail in this section.

The results presented in Fig. 13a reveal that the degradation of CAP in the dark phase remained consistent across all scavenger tests, as scavengers primarily influence ROS generation pathways only upon Fe_3O_4 light activation. In contrast, under irradiation, the mineralization of CAP varied depending on the scavenger used, indicating that hydroxyl radicals play a dominant role in the mineralization process (Fig. 13b). These radicals are generated through the synergistic interaction of Fe^{3+}/Fe^{2+} in magnetite, hydrogen peroxide, and, to a lesser extent, photoinduced holes from Fe_3O_4 under solar light. This mechanism was further supported by the negligible mineralization observed in the presence of IPA. Notably, the direct photolysis of H_2O_2 ($H_2O_2 + h\nu \rightarrow 2$ •OH) did not contribute to CAP degradation, as confirmed by control experiments

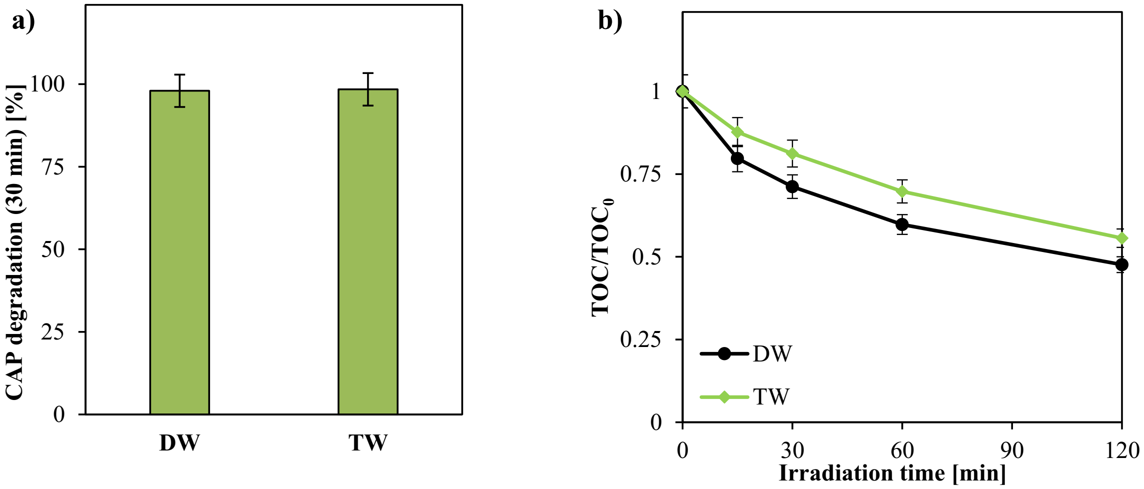

Fig. 12. (a) CAP degradation efficiency after 30 min of dark-phase treatment using Fe^0(3.3 %)/Fe_3O_4(1.6 %)/USY 360 in distilled water (DW) and tap water (TW); (b) CAP mineralization under solar irradiation for 120 min (expressed as TOC/TOC_0, where TOC is the residual total organic carbon at time t and TOC_0 is the initial value). Experimental conditions: $[CAP]_0$ = 25 ppm, $[H_2O_2]$ = 0.12 g L^{-1}, catalyst dosage = 1.5 g L^{-1}, pH = 4.

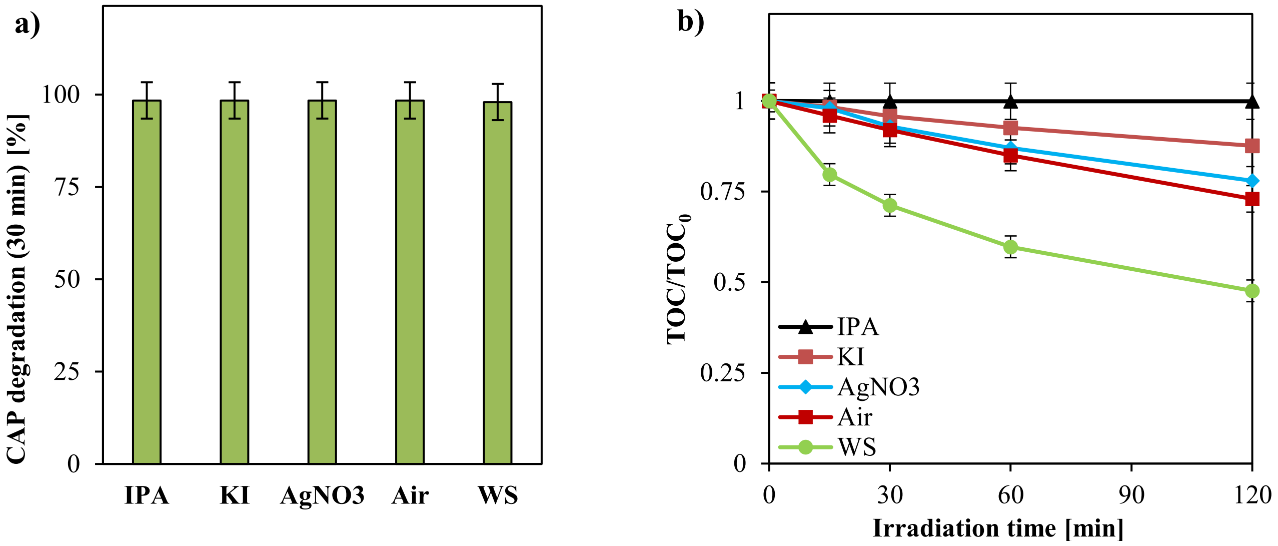

Fig. 13. (a) CAP degradation efficiency after 30 min in the dark phase using the Fe^0(3.3 %)/Fe_3O_4(1.6 %)/USY 360 catalyst in the presence of various scavengers; (b) CAP mineralization under solar irradiation (expressed as TOC/TOC$_0$, where TOC is the residual total organic carbon at time t and TOC$_0$ the initial value). Experimental Conditions: $[CAP]_0 = 25$ ppm, catalyst dosage = 1.5 g L^{-1}, $[H_2O_2] = 0.12$ g L^{-1}, pH = 4.

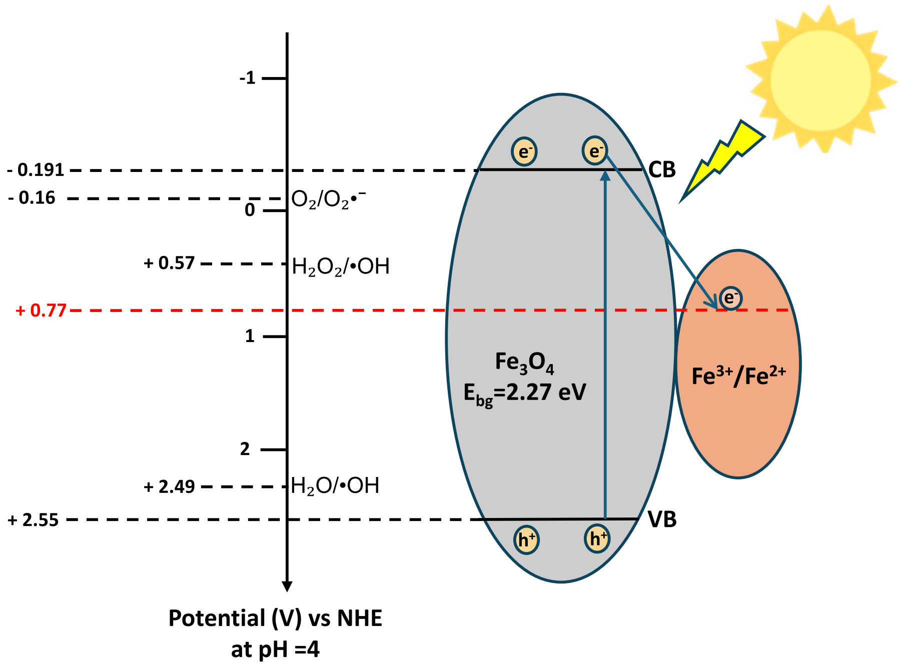

Fig. 14. Schematic illustration of the proposed mechanism for charge carrier generation and reactive oxygen species (ROS) formation on the Fe_3O_4 surface under solar irradiation.

without photocatalyst (Fig. 7b). Since H_2O_2 photodissociation requires high-energy UV radiation ($\lambda < 380$ nm), solar irradiation alone was insufficient to drive this reaction [78]. Furthermore, experiments conducted under continuous air supply demonstrated that superoxide radical anions hindered the oxidation of CAP and its intermediates. The introduction of air promoted $O_2{\bullet}^-$ formation, which not only generated less reactive hydroperoxide radicals but also competed for electrons, impeding the regeneration of Fe^{2+} [26].

The photocatalytic mineralization mechanism of CAP over the Fe^0(3.3 %)/Fe_3O_4(1.6 %)/USY 360 composite can be rationalized by examining its electronic band structure and the thermodynamic feasibility of ROS generation.

According to Mulliken electronegativity theory and considering the Ebg value of Fe_3O_4 in the Fe^0(3.3 %)/Fe_3O_4(1.6 %)/USY 360 (2.27 eV, Fig. S7), the estimated conduction band (E_{CB}) and valence band (E_{VB}) potentials for Fe_3O_4 at pH = 4 are approximately −0.191 V and + 2.55 V vs NHE at pH = 4, respectively (Fig. 14).

Under irradiation, the electrons in the VB of Fe_3O_4 are promoted to the CB (Eq. (11)). In the absence of oxygen in the reaction medium, the H_2O_2 added at the beginning of irradiation can be decomposed on the Fe_3O_4 surface into highly oxidative hydroxyl radicals (•OH) in acidic conditions (Eq. (12)), owing to the favorable redox potential of the $H_2O_2/{\bullet}OH$ pair (+0.57 V vs. NHE at pH = 4 [79]) relative to the E_{CB} value (Fig. 14). Furthermore, the valence band holes of Fe_3O_4 possess sufficient oxidizing power to convert water directly into hydroxyl radicals (Eq. (13)) ($H_2O/{\bullet}OH$ = +2.49 V vs. NHE at pH = 4, Fig. 14), further contributing to CAP mineralization.

Simultaneously, in the photo-Fenton mechanism, Fe^{2+} species generated from Fe^0 oxidation during the dark phase (Eq. (4)) react with H_2O_2 to produce •OH and Fe^{3+} (Eq. (14)) [80,81]. The photogenerated electrons from Fe_3O_4 can then reduce Fe^{3+} back to Fe^{2+} (Eq. (15)) [80,81]. This process is thermodynamically favored, given the redox potential of the Fe^{3+}/Fe^{2+} couple (+0.77 V vs. NHE) [26,74], which is more positive than the conduction band potential of Fe_3O_4 (Fig. 14). This facilitates continuous Fe^{3+}/Fe^{2+} cycling and suppresses electron–hole recombination, thereby enhancing photo-Fenton efficiency. In addition, Fe^{3+} can also be photoreduced by water under solar irradiation, further contributing to the regeneration of Fe^{2+} species and sustaining the catalytic cycle [82] (Eq. (16)). The hydroxyl radicals thus generated are responsible for the mineralization of intermediates (Eq. (17)), which themselves originate from the dehalogenation of CAP promoted by Fe^0 (Eq. (5)).

In contrast, when oxygen is present in the system, the photogenerated electrons in the CB of Fe_3O_4 can reduce molecular oxygen to superoxide, since the redox potential of the $O_2/O_2^{\bullet-}$ couple (−0.16 V vs. NHE [79]) is more positive than the E_{CB} of Fe_3O_4 (Fig. 14). In this scenario, electrons in the CB of Fe_3O_4 are no longer available to drive the Fe^{3+}/Fe^{2+} cycling under irradiation. This mechanism is consistent with the depletion of mineralization efficiency observed in experiments conducted under air bubbling (Fig. 13b).

$$Fe_3O_4 + h\nu \rightarrow h^+ + e^- \tag{11}$$

$$H_2O_2 + e^- + H^+ \rightarrow \dot{O}H + H_2O \tag{12}$$

$$H_2O + h^+ \rightarrow \dot{O}H + H^+ \tag{13}$$

$$Fe^{2+} + H_2O_2 \rightarrow Fe^{3+} + \dot{O}H + OH^- \tag{14}$$

$$Fe^{3+} + e^- \rightarrow Fe^{2+} \tag{15}$$

$$Fe^{3+} + H_2O + h\nu \rightarrow Fe^{2+} + \dot{O}H + H^+ \tag{16}$$

$$\text{Intermediates} + \dot{O}H \rightarrow CO_2 + H_2O \tag{17}$$

Although a formal heterojunction structure was not explicitly designed in this system, the co-presence of Fe^0 and Fe_3O_4 promotes interfacial charge transfer under irradiation, enabling redox cycling between Fe^{3+} and Fe^{2+}. This mimics a heterojunction-like behavior, supported by estimated band energetics and radical inhibition studies. However, further in-depth characterization and DFT simulations will be required to definitively determine the electron transfer pathway and classify the nature of the heterostructure.

3.3.7. *Electric energy consumption analysis*

To evaluate the energy efficiency of the process, the specific electrical energy consumption ($E_{E/O}$) required to degrade 90 % of chloramphenicol (CAP) in 1 m^3 of contaminated water was estimated under optimized conditions. The calculation followed the methodology proposed by Bolton et al. [83], as expressed in Eq. (18):

$$E_{E/O} = \frac{P\, t_{90\%}\, 1000}{V\, 60 \ln\left(\frac{C(t_0)}{C(t_{90\%})}\right)} \tag{18}$$

where $E_{E/O}$ is the electric energy consumption (kWh), P is the nominal power of the light source (kW), $t_{90\%}$ is the irradiation time to achieve 90 % mineralization of CAP (min), V is the volume of treated solution (L), $C(t_0)$ is the initial CAP concentration (ppm) at the start of irradiation, and $C(t_{90\%})$ is the CAP concentration (ppm) at time $t_{90\%}$.

In this study, comparative analysis was carried out by examining previously published photocatalytic and photo-Fenton processes used for CAP removal (Table 4).

The resulting $E_{E/O}$ values confirmed the superior energy efficiency of the Fe^0(3.3 %)/Fe_3O_4(1.6 %)/USY system developed in this work. Among all reviewed processes, the current catalyst demonstrated the lowest energy demand, highlighting its potential for sustainable wastewater remediation, especially for pharmaceutical and hospital pollutants.

4. Conclusions

This study demonstrates the high efficiency of a Fe^0(3.3 %)/Fe_3O_4(1.6 %)/USY 360 composite catalyst for the solar photo-Fenton degradation and mineralization of chloramphenicol (CAP) under mildly acidic conditions (pH = 4).

We successfully modulated the metallic iron to magnetite ratio by exploiting variations in the Si/Al ratio of the parent USY zeolites (i.e., USY360 with an atomic Si/Al ratio of 6.9 and USY390 with an atomic Si/Al ratio of 385) and by precisely controlling the heat treatment temperature applied to the impregnated zeolite.

The presence of zero-valent iron was essential for promoting CAP degradation in the dark phase via reductive pathways of the target pollutant. Under solar irradiation, magnetite (Fe_3O_4) played a pivotal role in promoting CAP mineralization by facilitating Fe^{3+}/Fe^{2+} redox cycling and acting as an electron mediator, enhancing charge separation and supporting continuous •OH generation. The combined effect of Fe^0 and Fe_3O_4 ensured both rapid degradation in dark conditions and effective mineralization of CAP intermediates under irradiation.

The optimal catalyst dosage (1.5 g L^{-1}) and H_2O_2 concentration (0.12 g L^{-1}) enabled up to 98 % CAP degradation and 52 % TOC removal in 120 min, with excellent reusability over five consecutive cycles and no detectable iron leaching. The efficiency of the process declined markedly at near-neutral pH (6.5), confirming the critical role of acidic conditions in maintaining the oxidative potential of hydroxyl radicals.

Although the system remained effective in real water matrices, the presence of anions such as Cl^-, NO_3^-, and PO_4^{3-} reduced mineralization due to radical scavenging. Mechanistic analyses confirmed that hydroxyl

Table 4

Comparison of the electric energy consumption for the CAP removal of 90 % in 1 m^3 of solution with the optimal operative conditions and the other works reported in the literature.

Process	Sample	Type of light	P [kW]	$t_{90\%}$ [min]	V [L]	$E_{E/O}$ [kWh m^{-3}]	$c_{H_2O_2}$ [g L^{-1}]	Ref.
Photocatalysis	TiO_2 P-25	UV-A	0.45	19.68	0.2	320.5	0	[84]
Photocatalysis	PPy-$ZnIn_2S_4$	Visible light	0.1	14	0.4	25.3	0	[85]
Photocatalysis	ZnO	UV-A	0.018	1081.818	0.15	939.7	0	[10]
Photocatalysis	SrF_3O_3-x/g-C_3N_4	Visible light	0.15	945.578	0.1	10,266.5	0	[7]
Photocatalysis	$Ce(MoO_4)_2$/GO	Visible light	0.5	25	0.1	904.8	0	[11]
Photocatalysis	ATP/Cu_2O/Cu/g-C_3N_4	Solar light	0.3	293.445	0.5	1274.4	0	[8]
Photocatalysis	Fe-Er-Bi_5O_7I	Visible light	0.45	297.187	0.05	19,360	0	[9]
Photo-Fenton	$FeSO_4$	UV-A	0.4	20	0.85	68.1	0.4	[12]
Photo-Fenton	Fe^{3+}(GO)	Visible light	0.4	22.226	0.1	643.5	0.02	[13]
Photo-Fenton	FSA (4 % Fe^0)	Visible light	0.03	19.125	0.01	415.3	0.034	[14]
Photo-Fenton	Fe^0(3.3 %)/ Fe_3O_4(1.6 %)/USY 360	Solar light	0.032	4.515	0.1	10.5	0.12	Our System

radicals were the main oxidative species responsible for CAP mineralization, generated via photo-induced pathways.

Finally, energy efficiency calculations showed a competitive $E_{E/O}$ value under optimized conditions, positioning this system as a promising, scalable solution for the treatment of CAP-contaminated waters.

CRediT authorship contribution statement

Nicola Morante: Writing – original draft, Investigation, Data curation. **Antonello Marocco:** Writing – original draft, Investigation, Data curation. **Viviana Monfreda:** Investigation, Data curation. **Alessandro Padua:** Investigation, Data curation. **Mattia Sisti:** Investigation, Data curation. **Rossella Arletti:** Visualization, Formal analysis, Data curation. **Diana Sannino:** Visualization. **Michele Pansini:** Methodology, Conceptualization. **Serena Esposito:** Writing – review & editing, Supervision, Conceptualization. **Vincenzo Vaiano:** Writing – review & editing, Methodology, Investigation, Data curation, Conceptualization.

Declaration of competing interest

The authors declare that they have no known competing financial interests or personal relationships that could have appeared to influence the work reported in this paper.

Appendix A. Supplementary data

Supplementary data to this article can be found online at https://doi.org/10.1016/j.jwpe.2025.108938.

Data availability

Data will be made available on request.

References

[1] C. Yan, Y. Yang, J. Zhou, M. Liu, M. Nie, H. Shi, L. Gu, Antibiotics in the surface water of the Yangtze Estuary: occurrence, distribution and risk assessment, Environ. Pollut. 175 (2013) 22–29.

[2] J. Lin, K. Zhang, L. Jiang, J. Hou, X. Yu, M. Feng, C. Ye, Removal of chloramphenicol antibiotics in natural and engineered water systems: review of reaction mechanisms and product toxicity, Sci. Total Environ. 850 (2022) 158059.

[3] C. Li, F. Luo, H. Duan, F. Dong, X. Chen, M. Feng, Z. Zhang, L. Cizmas, V.K. Sharma, Degradation of chloramphenicol by chlorine and chlorine dioxide in a pilot-scale water distribution system, Sep. Purif. Technol. 211 (2019) 564–570.

[4] A. Mancuso, O. Tammaro, F. Raffone, G. Cicero, O. Sacco, M. Pansini, V. Vaiano, S. Esposito, Enhanced adsorptive removal of chloramphenicol from water by highly defective MOF-808 nanocrystals fine-tuned with reliable synthesis strategy: mechanism insight by equilibrium, kinetics and molecular dynamics simulations, Chem. Eng. J. 504 (2025) 158698.

[5] I.M. Gonzaga, C.V. Almeida, L.H. Mascaro, A critical review of photo-based advanced oxidation processes to pharmaceutical degradation, Catalysts 13 (2023) 221.

[6] M. Qutob, S. Alshehri, F. Shakeel, P. Alam, M. Rafatullah, An insight into the role of experimental parameters in advanced oxidation process applied for pharmaceutical degradation, Environ. Sci. Pollut. Res. 31 (2024) 26452–26479.

[7] H.P. Lin, C.C. Chen, W.W. Lee, Y.-Y. Lai, J.Y. Chen, Y.Q. Chen, J.Y. Fu, Synthesis of a $SrFeO_{3-x}/g\text{-}C_3N_4$ heterojunction with improved visible-light photocatalytic activities in chloramphenicol and crystal violet degradation, RSC Adv. 6 (2016) 2323–2336.

[8] S. Zuo, Y. Chen, W. Liu, C. Yao, X. Li, Z. Li, C. Ni, X. Liu, A facile and novel construction of attapulgite/Cu_2O/Cu/g-C_3N_4 with enhanced photocatalytic activity for antibiotic degradation, Ceram. Int. 43 (2017) 3324–3329.

[9] Y. Liu, G. Zhu, J. Gao, R. Zhu, M. Hojamberdiev, C. Wang, X. Wei, P. Liu, A novel synergy of Er^{3+}/Fe^{3+} co-doped porous Bi_5O_7I microspheres with enhanced photocatalytic activity under visible-light irradiation, Appl. Catal. Environ. 205 (2017) 421–432.

[10] I. Pronin, N. Kaneva, A. Bozhinova, I. Averin, K. Papazova, D.T. Dimitrov, V. Moshnikov, Photocatalytic oxidation of pharmaceuticals on thin nanostructured zinc oxide films, Kinet. Catal. 55 (2014) 167–171.

[11] R. Karthik, J. Vinoth Kumar, S.-M. Chen, C. Karuppiah, Y.-H. Cheng, V. Muthuraj, A study of electrocatalytic and photocatalytic activity of cerium molybdate nanocubes decorated graphene oxide for the sensing and degradation of antibiotic drug chloramphenicol, ACS Appl. Mater. Interfaces 9 (2017) 6547–6559.

[12] A.G. Trovó, V.A. de Paiva, A.E. Machado, C.A. de Oliveira, R.O. Santos, Degradation of the antibiotic chloramphenicol by photo-Fenton process at lab-scale and solar pilot plant: kinetic, toxicity and inactivation assessment, Sol. Energy 97 (2013) 596–604.

[13] F. Cheng, P. Zhou, Y. Liu, X. Huo, J. Zhang, Y. Yuan, H. Zhang, B. Lai, Y. Zhang, Graphene oxide mediated Fe (III) reduction for enhancing Fe (III)/H_2O_2 Fenton and photo-Fenton oxidation toward chloramphenicol degradation, Sci. Total Environ. 797 (2021) 149097.

[14] L. Skvortsova, K. Kazantseva, K. Bolgaru, K. Dychko, Visible light-induced oxidative degradation of chloramphenicol by iron-containing ceramic-metal composites, Rev. Adv. Chem. 12 (2022) 289–295.

[15] J.P. Ribeiro, M.I. Nunes, Recent trends and developments in Fenton processes for industrial wastewater treatment–a critical review, Environ. Res. 197 (2021) 110957.

[16] F. Machado, A. Teixeira, L. Ruotolo, Critical review of Fenton and photo-Fenton wastewater treatment processes over the last two decades, Int. J. Environ. Sci. Technol. 20 (2023) 13995–14032.

[17] M. Periyasamy, S. Sain, U. Sengupta, M. Mandal, S. Mukhopadhyay, A. Kar, Bandgap tuning of photo fenton-like Fe 3 O 4/C catalyst through oxygen vacancies for advanced visible light photocatalysis, Mater. Adv. 2 (2021) 4843–4858.

[18] M.D. Permana, T. Takei, A.A. Khatun, D.R. Eddy, N. Saito, N. Kumada, Effect of wavelength in light irradiation for Fe2+/Fe3+ redox cycle of Fe_3O_4/g-C_3N_4 in photocatalysis and photo-Fenton systems, J Photochem Photobiol A Chem 457 (2024) 115876.

[19] Q. Li, Z. Chen, H. Wang, H. Yang, T. Wen, S. Wang, B. Hu, X. Wang, Removal of organic compounds by nanoscale zero-valent iron and its composites, Sci. Total Environ. 792 (2021) 148546.

[20] T.A. Bruton, B.F. Pycke, R.U. Halden, Effect of nanoscale zero-valent iron treatment on biological reductive dechlorination: a review of current understanding and research needs, Crit. Rev. Environ. Sci. Technol. 45 (2015) 1148–1175.

[21] A. Cardito, L. Albarano, O. Sacco, V. Vaiano, M. Lettieri, G. Libralato, G. Lofrano, M. Carotenuto, Removal and toxicity effects of chloramphenicol and acid orange solutions using zero-valent iron nanoparticles, J Water Process Eng 69 (2025) 106868.

[22] A. Cardito, M. Carotenuto, O. Sacco, L. Albarano, V. Vaiano, P. Iannece, G. Libralato, V.R. Spica, G. Lofrano, UV light assisted degradation of acid orange azo dye by ZVI-ZnS and effluent toxicity effects, Environ. Pollut. 343 (2024) 123226.

[23] O. Sacco, V. Vaiano, W. Navarra, C. Daniel, S. Pragliola, V. Venditto, Catalytic system based on recyclable Fe^0 and ZnS semiconductor for UV-promoted degradation of chlorinated organic compounds, Sep. Purif. Technol. 270 (2021) 118830.

[24] F. Sannino, S. Ruocco, A. Marocco, S. Esposito, M. Pansini, Cyclic process of simazine removal from waters by adsorption on zeolite HY and its regeneration by thermal treatment, J. Hazard. Mater. 229 (2012) 354–360.

[25] M. Pansini, F. Sannino, A. Marocco, P. Allia, P. Tiberto, G. Barrera, M. Polisi, E. Battista, P.A. Netti, S. Esposito, Novel process to prepare magnetic metal-ceramic nanocomposites from zeolite precursor and their use as adsorbent of agrochemicals from water, J. Environ. Chem. Eng. 6 (2018) 527–538.

[26] O. Tammaro, N. Morante, A. Marocco, M. Fontana, M. Castellino, G. Barrera, P. Allia, P. Tiberto, R. Arletti, R. Fantini, V. Vaiano, S. Esposito, D. Sannino, M. Pansini, The beneficial role of nano-sized Fe3O4 entrapped in ultra-stable Y zeolite for the complete mineralization of phenol by heterogeneous photo-Fenton under solar light, Chemosphere 345 (2023) 140400.

[27] C. Weidenthaler, B. Zibrowius, J. Schimanke, Y. Mao, B. Mienert, E. Bill, W. Schmidt, Oxidation behavior of ferrous cations during ion exchange into zeolites under atmospheric conditions, Microporous Mesoporous Mater. 84 (2005) 302–317.

[28] C. Baerlocher, L.B. McCusker, D.H. Olson, Atlas of Zeolite Framework Types, Elsevier, 2007.

[29] J. Parise, D. Corbin, L. Abrams, D. Cox, Structure of dealuminated Linde Y-zeolite; Si139. 7Al52. 3O384 and Si173. 1Al18. 9O384: presence of non-framework Al species, Cryst. Struct. Commun. 40 (1984) 1493–1497.

[30] L. Kong, Z. Jiang, H.H.-C. Lai, T. Xiao, P.P. Edwards, Does noble metal modification improve the photocatalytic activity of BiOCl? Prog. Nat. Sci.: Mater. Int. 23 (2013) 286–293.

[31] P. Ghamari Kargar, B. Maleki, M. Ghani, Ag/GO/Fe3O4/γ-Fe2O3 nanocomposite for green-light-driven photocatalytic oxidation of 5-hydroxymethylfurfural to 5-hydroxymethyl-2-furancarboxylic acid, ACS Appl. Nano Mater. 7 (2024) 8765–8782.

[32] G. Eisenberg, Colorimetric determination of hydrogen peroxide, Ind. Eng. Chem. Anal. Ed. 15 (1943) 327–328.

[33] A. Colantuono, S.D. Vecchio, G. Mascolo, M. Pansini, Thermal shrinkage of various cation forms of zeolite A, Thermochim. Acta 296 (1997) 59–66.

[34] D. Xu, H. Lv, B. Liu, Encapsulation of metal nanoparticle catalysts within mesoporous zeolites and their enhanced catalytic performances: a review, Front. Chem. 6 (2018) 550.

[35] C. Wang, S. Leng, H. Guo, J. Yu, W. Li, L. Cao, J. Huang, Quantitative arrangement of Si/Al ratio of natural zeolite using acid treatment, Appl. Surf. Sci. 498 (2019) 143874.

[36] J. Zhang, X. Tang, H. Yi, Q. Yu, Y. Zhang, J. Wei, Y. Yuan, Synthesis, characterization and application of Fe-zeolite: a review, Appl. Catal. Gen. 630 (2022) 118467.

[37] P. Xiao, H. Toyoda, Y. Wang, K. Nakamura, S. Bekhti, R. Osuga, M. Nishibori, H. Gies, T. Yokoi, Roles of acidic proton for Fe-containing zeolite in direct oxidation of methane, ACS Catal. 14 (2024) 17434–17444.

[38] P. Nidheesh, R. Gandhimathi, S. Velmathi, N. Sanjini, Magnetite as a heterogeneous electro Fenton catalyst for the removal of rhodamine B from aqueous solution, RSC Adv. 4 (2014) 5698–5708.

[39] K.J. Kim, H.S. Lee, M.H. Lee, S.H. Lee, Comparative magneto-optical investigation of d–d charge–transfer transitions in Fe_3O_4, $CoFe_2O_4$, and $NiFe_2O_4$, J. Appl. Phys. 91 (2002) 9974–9977.

[40] A. Mancuso, O. Sacco, V. Vaiano, B. Bonelli, S. Esposito, F.S. Freyria, N. Blangetti, D. Sannino, Visible light-driven photocatalytic activity and kinetics of Fe-doped TiO_2 prepared by a three-block copolymer templating approach, Materials 14 (2021) 3105.

[41] J.-H. Yang, C.-P. Wang, B.-H. Chen, M.H. Huang, Growth of Fe_3O_4 truncated cubes and rhombic dodecahedra showing interior lattice and magnetic behavior variations, Inorg. Chem. 64 (2025) 8659–8667.

[42] G. Sorbino, O. Tammaro, A. Padua, A. Basco, S. Scognamiglio, M. Sisti, R. Arletti, A. Marocco, M. Pansini, G. Landi, Unveiling the role of Ni nanometric particles in ultra-stable hierarchically porous Y zeolite to drive methane steam reforming and CO_2 hydrogenation, Int. J. Hydrogen Energy 103 (2025) 887–900.

[43] J. Zhao, G. Wang, L. Qin, H. Li, Y. Chen, B. Liu, Synthesis and catalytic cracking performance of mesoporous zeolite Y, Catal. Commun. 73 (2016) 98–102.

[44] W. Schwieger, A.G. Machoke, T. Weissenberger, A. Inayat, T. Selvam, M. Klumpp, A. Inayat, Hierarchy concepts: classification and preparation strategies for zeolite containing materials with hierarchical porosity, Chem. Soc. Rev. 45 (2016) 3353–3376.

[45] J. Rouquerol, P. Llewellyn, F. Rouquerol, Is the BET equation applicable to microporous adsorbents?, in: Studies in Surface Science and Catalysis Elsevier, 2007, pp. 49–56.

[46] A. Ladavos, A. Katsoulidis, A. Iosifidis, K. Triantafyllidis, T. Pinnavaia, P. Pomonis, The BET equation, the inflection points of N_2 adsorption isotherms and the estimation of specific surface area of porous solids, Microporous Mesoporous Mater. 151 (2012) 126–133.

[47] B. Ma, B. Lu, H. Tang, H. Wang, Z. Bian, Square-wave pulsed potential driven electrocatalytic degradation of 4-chlorophenol using Fe-Ni/rGO/PPy@ NF three dimensional electrode, J. Hazard. Mater. 480 (2024) 136054.

[48] L. Wu, X. Yan, L. Yang, S. Shen, Y. Li, S. Yang, L. He, Y. Chen, S. Yang, Z. Zhang, Simultaneous efficient degradation and dechlorination of chloramphenicol using UV/sulfite reduction: mechanisms and product toxicity, Chem. Eng. J. 452 (2023) 139161.

[49] J. Yu, X. Hou, X. Hu, H. Yuan, J. Wang, C. Chen, Efficient degradation of chloramphenicol by zero-valent iron microspheres and new insights in mechanisms, Appl. Catal. Environ. 256 (2019) 117876.

[50] Z. Liang, C. Jiang, Y. Li, Y. Liu, J. Yu, T. Zhang, P.J. Alvarez, W. Chen, Single-atom iron can steer atomic hydrogen toward selective reductive dechlorination: implications for remediation of chlorinated solvents-impacted groundwater, Environ. Sci. Technol. 58 (2024) 11833–11842.

[51] M. Gheju, Mechanisms of contaminant removal with metallic iron (Fe0): a comprehensive and critical review, Sep. Purif. Technol. 364 (2025) 132503–132522.

[52] Y. Dai, W. Du, C. Jiang, W. Wu, Y. Dong, L. Duan, S. Sun, B. Zhang, S. Zhao, Enhanced reductive degradation of chloramphenicol by sulfidated microscale zero-valent iron: sulfur-induced mechanism, competitive kinetics, and new transformation pathway, Water Res. 233 (2023) 119743.

[53] J. Xiao, S. Guo, D. Wang, Q. An, Fenton-like reaction: recent advances and new trends, Chem. Eur. J. 30 (2024) e202304337.

[54] Y. Bai, X. Sun, Y. Dang, S. Yu, J.-J. Zhu, Y. Zhou, A self-circulating electro-Fenton-like process over Fe_3O_4–CaO_2 cathode for highly efficient degradation of levofloxacin, Chemosphere 313 (2023) 137520.

[55] M.A. Khoj, N.S. Awwad, H.A. Ibrahium, A.M. Awad, A.F. Hassan, Enhanced adsorption and photo-Fenton degradation of diazinon pesticide utilizing nanomagnetite/graphene oxide composite: kinetic and thermodynamic studies, J. Inorg. Organomet. Polym. Mater. 34 (2024) 3483–3500.

[56] C. Udhayakeerthana, B. Palanivel, K. Vignesh, T. Kalaivani, An enhanced optical response and interfacial charge separation of rGO supported Cu^{2+} doped Co_3O_4 heterojunction for photo-Fenton-like activity, ChemistrySelect 9 (2024) e202400375.

[57] Y. Zheng, J. Fan, J. Cui, B. Yang, Green synthesis of ZnFe2O4@ BC nanocrystals using pomelo peel waste for photo-Fenton degradation of dye under visible light, ChemistrySelect 9 (2024) e202302952.

[58] Q. Li, G. Wei, Y. Yang, L. Gao, L. Zhang, Z. Li, X. Huang, J. Gan, Novel step-scheme red mud based Ag_3PO_4 heterojunction photocatalyst with enhanced photocatalytic performance and stability in photo-Fenton reaction, Chem. Eng. J. 424 (2021) 130537.

[59] H.A. El-Gawad, M.Y. Ghaly, N. El Hussieny, M. Abdel Kreem, Y. Reda, Novel collector design and optimized photo-Fenton model for sustainable industry textile wastewater treatment, Sci. Rep. 14 (2024) 8573.

[60] Y. San juan-Garisado, F. Luna-Guevara, P.A. Herrera, J. Soto-Paz, J.D. Alvarez-Trujillo, C. Mejia-Parada, B.A. Parra-Orobio, Optimization of the photo-Fenton process for the effective removal of chemical oxygen demand and phenols in portable toilet wastewater: a treatment study under real world conditions, Heliyon 10 (e35286) (2024).

[61] F. Ge, X. Li, M. Wu, H. Ding, X. Li, A type II heterojunction α-Fe_2O_3/g-C_3N_4 for the heterogeneous photo-Fenton degradation of phenol, RSC Adv. 12 (2022) 8300–8309.

[62] N. Thomas, D.D. Dionysiou, S.C. Pillai, Heterogeneous Fenton catalysts: a review of recent advances, J. Hazard. Mater. 404 (2021) 124082.

[63] Y. Chen, C.J. Miller, T.D. Waite, Heterogeneous Fenton chemistry revisited: mechanistic insights from ferrihydrite-mediated oxidation of formate and oxalate, Environ. Sci. Technol. 55 (2021) 14414–14425.

[64] M. Sayed, A. Khan, S. Rauf, N.S. Shah, F. Rehman, A.A. Al-Kahtani, J.A. Khan, J. Iqbal, G. Boczkaj, I. Gul, Bismuth-doped nano zerovalent iron: a novel catalyst for chloramphenicol degradation and hydrogen production, ACS Omega 5 (2020) 30610–30624.

[65] M. Pansini, G. Dell'Agli, A. Marocco, P.A. Netti, E. Battista, V. Lettera, P. Vergara, P. Allia, B. Bonelli, P. Tiberto, Preparation and characterization of magnetic and porous metal-ceramic nanocomposites from a zeolite precursor and their application for DNA separation, J. Biomed. Nanotechnol. 13 (2017) 337–348.

[66] P.A. Bizirtsakis, K. Anagnostopoulou, V.C. Sarasidis, P. Petsi, A. Moschona, K. V. Plakas, D.A. Lambropoulou, A comparative study of advanced oxidation processes for the removal of the antibiotic sulfadoxine from water—transformation products and toxicity, Appl. Sci. 15 (2025) 793.

[67] N. Morante, K. Monzillo, V. Vaiano, Z.C. Kadirova, D. Sannino, Synthesis and characterization of a novel sol–gel-derived Ni-doped TiO2 photocatalyst for rapid visible light-driven mineralization of paracetamol, Nanomaterials 15 (530) (2025).

[68] C. Liu, L. Yan, L. Zhu, Y. Yu, Y. Tai, Y. Yu, Q. Liu, L. Li, Highly efficient removal of tetrabromobisphenol A by Fenton degradation with iron-modulated zeolite under nanoconfinement, Colloids Surf. A Physicochem. Eng. Asp. 698 (2024) 134537.

[69] H. Li, D. Li, C. Yin, F. Xu, Construction of magnetic FeP/CdS composites as photo-Fenton-like catalysts to realize high-efficiency degradation of tetracycline hydrochloride, ChemCatChem 17 (2025) e202401364.

[70] J. Wang, S. Wang, Effect of inorganic anions on the performance of advanced oxidation processes for degradation of organic contaminants, Chem. Eng. J. 411 (2021) 128392.

[71] N. Morante, V. Folliero, F. Dell'Annunziata, N. Capuano, A. Mancuso, K. Monzillo, M. Galdiero, D. Sannino, G. Franci, Characterization and photocatalytic and antibacterial properties of Ag-and TiOx-based (x= 2, 3) composite nanomaterials under UV irradiation, Materials 17 (2024) 2178.

[72] C. Chen, W. Gao, H. Fan, X. Huang, Z. Tong, Facile single-step synthesis of ZnFe2O4@ biochar for synergistic adsorption and photo-Fenton degradation of RB and RBR binary dyes, J. Taiwan Inst. Chem. Eng. 163 (2024) 105641.

[73] L. Ding, Y. Hou, H. Liu, J. Peng, Z. Cao, Y. Zhang, B. Wang, X. Cao, Y. Chang, T. Wang, Alcohols as scavengers for hydroxyl radicals in photocatalytic systems: reliable or not? Acs Es&t Water 3 (2023) 3534–3543.

[74] V.P. Ulin, N.V. Ulin, F.Y. Soldatenkov, Anodic processes in the chemical and electrochemical etching of Si crystals in acid-fluoride solutions: pore formation mechanism, Semiconductors 51 (2017) 458–472.

[75] N.M. Abadiah, D. Yuliantika, Y.A. Hariyanto, R.E. Saputro, A. Taufiq, S. Soontaranoon, Nanostructure, band gap, and antibacterial activity of spinel Fe2MO4/OO magnetic fluids, in: IOP Conference Series: Earth and Environmental Science, IOP Publishing, 2019, p. 012064.

[76] H.-L. Hsu, L.S. Roselin, R. Savidha, R. Selvin, Enhanced photocatalytic performance of magnetite/TS-1 thin film for phenol degradation, J. Saudi Chem. Soc. 26 (2022) 101538.

[77] T.B. Mbuyazi, P.A. Ajibade, Photocatalytic degradation of eosin yellow and quinaldine red under visible light irradiation by magnetite nanoparticles, J. Mol. Struct. 1334 (2025) 141862.

[78] T.T. Aye, T.Y. Low, S.K. Sze, Nanosecond laser-induced photochemical oxidation method for protein surface mapping with mass spectrometry, Anal. Chem. 77 (2005) 5814–5822.

[79] W.H. Koppenol, D.M. Stanbury, P.L. Bounds, Electrode potentials of partially reduced oxygen species, from dioxygen to water, Free Radic. Biol. Med. 49 (2010) 317–322.

[80] M. Wu, X. Guo, Y. Cao, H. Yu, Z. Hu, Y. Yang, T. Yao, J. Wu, Cascading H_2O_2 photosynthesis and fenton reaction for self-sufficient photo-fenton reactions: a review of recent advances, Chem. Eng. J. 489 (2024) 151091–151117.

[81] B. Janani, V.V. Sre, A. Syed, A.M. Elgorban, I. Abid, L.S. Wong, S.S. Khan, Engineering defects and lattice disorientation in layered double hydroxides by coupling 2D-Co (OH) 2 platelets via pn heterojunction for enhanced photocatalytic degradation chloramphenicol, Colloids Surf. A Physicochem. Eng. Asp. 705 (2025) 135674.

[82] X. Zhang, Z. Chen, X. Li, Y. Wu, J. Zheng, Y. Li, D. Wang, Q. Yang, A. Duan, Y. Fan, Promoted electron transfer in Fe2+/Fe3+ co-doped BiVO4/Ag3PO4 S-scheme heterojunction for efficient photo-Fenton oxidation of antibiotics, Sep. Purif. Technol. 310 (2023) 123116.

[83] J.R. Bolton, J.E. Valladares, J.P. Zanin, W.J. Cooper, M.G. Nickelsen, D.C. Kajdi, n. Waite, C.N. Kurucz, Figures-of-merit for advanced oxidation technologies: a comparison of homogeneous UV/H2O2, heterogeneous UV/TiO2 and electron beam processes, J. Adv. Oxid. Technol. 3 (1998) 174–181.

[84] G. Lofrano, G. Libralato, R. Adinolfi, A. Siciliano, P. Iannece, M. Guida, M. Giugni, A.V. Ghirardini, M. Carotenuto, Photocatalytic degradation of the antibiotic chloramphenicol and effluent toxicity effects, Ecotoxicol. Environ. Saf. 123 (2016) 65–71.

[85] B. Gao, W. Chen, S. Dong, J. Liu, T. Liu, L. Wang, M. Sillanpää, Polypyrrole/ZnIn2S4 composite photocatalyst for enhanced mineralization of chloramphenicol under visible light, J Photochem Photobiol A Chem 349 (2017) 115–123.